Microwave-Assisted Synthesis of Cu@IrO2

Core-Shell Nanowires for Low-Temperature Methane Conversion

Kenna L. Salvatore¹, Kaixi Deng^{1,2}, Scott C. McGuire¹, Sha Tan¹, Ning Rui², Lihua Zhang³, José A. Rodriguez^{2,*}, and Stanislaus S. Wong^{1,*}

Email: jrodriguez@bnl.gov; stanislaus.wong@stonybrook.edu

¹Department of Chemistry, State University of New York at Stony Brook,

Stony Brook, NY 11794-3400

²Chemistry Division, Building 555, Brookhaven National Laboratory,

Upton, NY 11973

³Center for Functional Nanomaterials, Building 735, Brookhaven National Laboratory,
Upton, NY 11973

Abstract

A facile microwave-assisted synthesis was developed for the tunable fabrication of a Cu@IrO₂ core@shell nanowire motif. Experimental parameters, such as (i) reaction time, (ii) the method of addition of the Ir precursor, (iii) capping agent, (iv) reducing agent, as well as (v) the capping agent-to-reducing agent ratio, were subsequently optimized. The viability of other methods based on previously reported literature, such as refluxing, stirring, and physical sonication, was studied and compared with our optimized microwave-assisted protocol in creating our as-prepared materials. It should be noted that the magnitude of the IrO₂ shell could be tailored, based on varying the Cu: Ir ratio coupled with judicious variations in the amounts of capping agent and reducing agent. Structural characterization techniques, such as XRD, XPS, and HRTEM (including HRTEM-EDS), were used to analyze our Cu@IrO₂ motifs. Specifically, the shell could be reliably tailored from sizes of 10 nm, 8 nm, 6 nm, and 3.5 nm with corresponding Cu: Ir ratios of 10: 1, 15: 1, 20: 1, and 25: 1, respectively. Moreover, the structural integrity of the motifs was probed and found to have been maintained after not only heat treatment but also the post-methane conversion process, indicative of an intrinsically high stability. Both components within the CuO-IrO₂ interface were able to activate methane at temperatures between 400 to 500 K with a reduction of the associated metal cations ($Cu^{2+} \rightarrow$ Cu^{1+} ; $Ir^{4+} \rightarrow Ir^{3+}$) and the deposition of CH_x fragments on the surface, as clearly observed in the ambient-pressure XPS results. Thus, on the basis of their stability and chemical activity, these core-shell materials could be very useful for the catalytic conversion of methane into 'higher value' chemicals.

Keywords: microwave-assisted synthesis, copper, iridium oxide, core@shell architecture, methane activation, catalysis, spectroscopic characterization.

1. Introduction

Copper-based (Cu) materials have been well studied for the steam reforming of carbon products, such as ethanol and methane. ^{1,2} Copper alone usually exhibits a limited catalytic activity, but when dispersed onto a solid support, good performance metrics can be achieved. Previously studied Cu-based catalysts have focused on bulk Cu supported on various metal oxides, such as but not limited to CeO₂, ³ ZrO₂, ^{4,5} Al₂O₃, ⁶ and SiO₂, ⁷ in addition to copper zeolites. ⁸ As an example, in one study exploring the behavior of CeO₂ doped with different metal cations such as Mn, Fe, Ni, Co, and Cu, the CeO₂-CuO catalyst exhibited the best performance in terms of CO oxidation. Furthermore, the addition of Cu within metal-containing matrices, such as those based on Ni, to create reactive bimetallic species not only enhanced the activity and overall higher selectivity of the reaction but also improved catalyst stability and decreased undesirable coke deposition. ^{4,5,9,10} However, whereas Cu may improve activity and selectivity, the catalyst is adversely affected by increasing water pressure and temperature. ^{6,11}

This problem can in principle be mitigated by the presence of a metal oxide shell within the context of a rationally designed core@shell architectural motif. Previously reported core@shell catalysts for methane conversion processes have focused on nanoparticles comprised of metal cores, such as Pd, ¹² Ni, ^{13, 14} and Co, ¹⁵ coupled with metal oxide shells consisting of CeO₂, SiO₂, and Al₂O₃, as examples. These distinctive core@shell nanoparticles evinced not only an increased stability of the catalyst with minimized coke deposition but also a higher selectivity for methane. As an example, core@shell nanoparticulate catalysts for dry methane reforming have been reported with Cu in combination with Ni as the core coupled with a SiO₂ shell, ¹⁶ generated using a microemulsion method. The presence of the shell improved catalytic stability of the catalyst and prevented sintering at high temperatures. The addition of Cu in the

catalyst was also perceived to have improved upon the catalytic activity and selectivity. ¹⁶ As a second example, with a Mo-M/TiO₂ (with M = Cu, Co) structure used in the context of a microwave-assisted, methane bi-reforming reaction, the presence of Cu^0 appeared to not only promote microwave absorption but also increase catalytic activity. ¹⁷ Therefore, the use of Cu as the core of the catalyst is desirable, because of its proven capability to yield higher selectivity and activity. However, studies of Cu-containing core@shell catalysts, especially in the context of methane conversion, are fairly limited.

As also noted in previous studies, the metal oxide shell is itself conducive to favorable activity and stability. ¹² Whereas many metal oxide candidates have been explored as the shell component, few studies have specifically investigated iridium oxide (IrO₂). Ir-based catalysts are known to be more active and durable as opposed to conventional Ni-based formulations, and recently Ir has been reported to be more active than Rh for the steam reforming of methane, based on turnover data. ¹⁸ Furthermore, methane is known to chemisorb onto IrO₂. Specifically, the Ir⁴⁺ ion within the rutile IrO₂ (110) possesses empty d_z^2 orbitals to accept electron donation from the C-H σ -bond and a filled d_{xy} orbital to enable back-bonding to the C-H anti-bonding orbitals. ¹⁹ Not surprisingly, IrO₂ itself has been studied for methane conversion, and is able to cleave the C-H bond within a reasonably accessible temperature range, i.e. ~150 °C. ²⁰⁻²² While some reports have considered elemental Ir metal as the active catalyst, recent DFT modeling and experimental studies have suggested that IrO₂ nanoparticles possessed a higher CH₄ activation activity as compared with that of reduced Ir⁰ nanoparticles, with 7 nm diameter IrO₂ nanoparticles found to be capable of activating CH₄ at temperatures as low as -115 °C. ²³

Previous Cu-Ir core shell structures have evinced enhanced activity as compared with their counterparts (of different chemical compositions) for applications ranging from methane oxidation, water splitting, to the oxygen evolution reaction. $^{20,\,24\text{-}26}$ Furthermore, it has been shown that a previously reported CuO@IrO2 nanoparticle core@shell catalyst derived from a metal organic framework (MOF) gave rise to an advantageously high catalytic activity for the selective oxidation of methane to methanol. 20 Associated experimental data highlighted a methanol yield of 872 μ mol g_{cat}^{-1} at 150 $^{\circ}$ C for 3 hours, coupled with enhanced stability for 5 cycles with no apparent degradation of activity. 20 Therefore, we have chosen to use IrO2 as the metal oxide shell herein, as a result of these encouraging activity data.

Whereas prior work has tended to focus on a Cu@IrO₂ core@shell nanoparticulate catalyst, this paper will center on the use of a novel microwave-assisted method to produce a unique 1D Cu@IrO₂ core@shell nanowire. Specifically, our distinctive core@shell motif takes advantage of the use of an underlying 1D core for the first time; it is worth highlighting that to the best of our knowledge, all of the previous CuIr systems reported have been based essentially exclusively on the zero-dimensional (0D) nanoparticulate platform.^{20, 24, 25, 27} In our study herein, the use of an anisotropic 1D motif imparts a number of potentially discernible benefits, including enhanced electron diffusion and conductivity properties with implications for measurable enhancements in overall catalyst stability and electrochemical performance.²⁸ Finally, the motif incorporates not only the potential for a low-temperature methane activation on the IrO₂ surface but also the intrinsically high selectivity of the Cu core. As such, the development of this unique catalytic platform using a facile synthesis method should enable the design of a tunable catalyst for enhanced methane conversion performance.

Therefore, the elements of novelty of our reported catalyst can be summarized, as follows: (1) a novel microwave-assisted method for producing Cu@IrO₂ core@shell architectures; (2) a distinctive core@shell motif based on an underlying wire structure; (3) a

systematic correlation of experimental reaction parameters with the resulting structure (which has not been previously discussed with other Cu@Ir core@shell studies);²⁴⁻²⁶ coupled with (4) tunable IrO₂ shell sizes, achieved in practice by varying the Ir precursor concentration.

Specifically, we intend to not only optimize the microwave-assisted technique to generate a uniform and homogeneous Cu@IrO₂ core@shell motif but also enable the capability of modulating the thickness of the external IrO₂ shell to optimize catalyst performance.

To date, Cu core@shell materials have not been routinely generated using microwave irradiation. Hence, this paper will focus on the benefits of using a microwave-assisted method in their production. The advantages of the microwave process include (i) the speed of reaction, which is often measured in mere minutes as compared with the lengthier time (such as hours) of other protocols (such as hydrothermal reactions) in addition to (ii) its overall facile use at relatively lower temperatures without the need for either complex equipment or more challenging reaction conditions.²⁹ Furthermore, the microwave reaction profits from the capability of utilizing solvents, such as ethanol, which are characterized by a relatively high tangent factor. This means that (a) the amount of microwave energy that can be absorbed can be reasonably elevated, and that (b) the use of metals such as Cu and Ir can lead to an increased absorption of microwave energy, due to the production of favorable 'hot spot' regions within the reaction medium, which can enable the creation of the desired core@shell architecture.

Previous microwave-assisted methods for synthesizing Cu core@shell motif have reported on the use of hydrolysable precursors, such as titanium butoxide. ^{30,31} In the current scheme, our microwave-assisted procedure utilizes an intrinsically more stable metal chloride salt, whose activity can be tuned to some extent by the presence of a capping agent. Our strategy builds on prior work with CuIr-based materials, fabricated using other distinctive synthetic

processes, ranging from reflux-based methods^{24, 25, 32} to high-temperature treatments.²⁰ To highlight the feasibility of this approach, as an example, CuIr alloys have been generated with a reflux-based scheme, incorporating a MCl₃ (i.e., IrCl₃) precursor in combination with cetyltrimethylammonium chloride (CTAC), in which the presence of Cl⁻ ions may have stimulated (111) facet growth.²⁴

Nevertheless, these previous studies have not as yet demonstrated the ability to systematically control the magnitude of the outer IrO₂ shell. Therefore, our work herein will explore not only the utilization of various capping agents, such as oleic acid, oleylamine, cetyltrimethylammonium bromide, and polyvinylpyrrolidone, all of which had been previously tried out as viable candidates in analogous studies of other core@shell nanowire motifs, ³³⁻³⁵ but also the role of the capping agent, working in synergistic combination with reducing agents, such as ascorbic acid, in order to yield a pure and uniform shell.

In summary, a novel microwave-assisted method for synthesizing a novel and unique Cu@IrO₂ core@shell motif with control over size, uniformity, and composition has been developed by exploring parameters such as but not limited to (i) the reaction time, (ii) the method of Ir precursor addition, (iii) the capping agent identity, and (iv) the capping agent-to-reducing agent ratio. The size of the IrO₂ shell can be deliberatively tuned by controlling the corresponding amount of Ir precursor used in the reaction. That is, we propose that tailored changes in structure will enable improved performance for methane conversion. By means of comparison, other complementary synthesis methods, such as stirring, ³⁶ reflux, ³⁷ and physical sonication, ³⁸ based on previous literature reports, will also be explored and compared with the microwave-assisted technique, in order to ascertain the 'optimal' approach for producing the desired Cu@IrO₂ motifs. Nonetheless, we expect to demonstrate the advantages of the

microwave-assisted protocol for yielding chemically well-defined, catalytically active motifs.

Moreover, as we will show, as a demonstration of their practical viability, our core@shell structures are stable and able to activate methane in the range of 300-500 K, which is a key achievement, considering that few materials are capable of initiating methane activation. Overall, these observations are promising for the use of these architectural motifs as potential catalysts for the conversion of this C_1 hydrocarbon to high-value chemicals at moderate temperatures.

2. Experimental Methods: Synthesis, Characterization, and Reactivity Studies

- 2.1. Materials. Materials, including IrCl₃(anhydrous) (Sigma Aldrich, reagent grade), CuCl₂ 2 H₂O (Bakers Analyzed), D-glucose (anhydrous) (Fisher Scientific, Certified ACS), 1-hexadecylamine (Acros Organics, 90%), polyvinylpyrrolidone (MW = 40,000) (Sigma Aldrich, K 30), and hexadecyl trimethylammonium bromide (Sigma Aldrich, 98%), were used, as received. Solvents such as anhydrous ethanol (Beantown Chemical, denatured), *n*-hexane (Alfa Aesar, spectrophotometric grade, 95+%), chloroform (Alfa Aesar, ACS, 99.8%), and DI water were all utilized, as procured, without any additional purification protocols involved.
- **2.2. Experimental:** Copper Nanowires. The Cu nanowires were initially synthesized using a previously published hydrothermal method.³⁹ For this synthesis, 1.08 grams of CuCl₂ 2 H₂O (copper source), 6.90 grams of 1-hexadecylamine (HDA) (capping agent), and 2.0 grams of D-glucose (reducing agent) were added to 400 mL water and then stirred for over 12 hours overnight, until the solution turned into a light blue emulsion. Subsequently, the solution was added into Teflon autoclaves and then heated to 100°C for 12 hours. The as-prepared wires were then subjected to centrifugation with thorough washing for several times with a combination of hydrophilic solvent (water) and hydrophobic solvent (chloroform/hexane) in order to

simultaneously remove both particles and excess 1-hexadecylamine. The resulting wires possessed diameters of roughly 20-50 nm with average lengths in microns. Our synthesis of Cu NWs yielded pure copper, as suggested by X-ray diffraction (XRD) results and illustrated by the red line with a high intensity [111] facet (shown in the XRD peak as ~43°) (**Figure S1**).

2.3. Synthesis of Cu@IrO₂ Core@shell structures To begin with, Cu NWs (20 mg, 0.315 mmol), IrCl₃ (5 mg, 0.016 mmol), ascorbic acid (0.1 g, 0.57 mmol), and polyvinylpyrrolidone (MW = 40,000, 20 mg) were dispersed in 1: 4 volume ratio of water: absolute ethanol with physical sonication for a period of 15 to 20 minutes. The solution was then heated with microwave radiation at 95 °C for 5 minutes. After cooling to room temperature, the successful outcome of a particular reaction was validated in terms of the formation of a reddish black solid within a green solution, which was separated by means of centrifugation and washed with ethanol, until a clear resulting supernatant was achieved.

2.4. Techniques for materials characterization

XRD: Samples were prepared by dispersing as-prepared materials in ethanol and then drop-casting them onto a zero-background holder (MTI Corporation, zero diffraction plate for XRD, B-doped, p-type Si, measuring 23.6 mm in diameter by 2 mm in thickness). Diffraction pattern data were obtained with a Rigaku Miniflex diffractometer, operating in the Bragg configuration and using Cu K α_1 irradiation ($\lambda = 1.54$ Å). Data were collected in the broad range of 20° to 80° at a scanning rate of 10° per minute.

SEM imaging: An ultra-high-resolution field emission Hitachi 4800 scanning electron microscope was used to characterize the apparent morphology of as-prepared core@shell structures. Samples were generated by dispersing powders in ethanol followed by drop casting aliquots onto a silicon wafer.

HRTEM: HRTEM images and accompanying energy dispersive X-ray spectroscopy (EDS) mapping data were collected on a JEOL 2100F instrument, operating at accelerating voltages of 200 kV with a beam size of 2 Å. Powders were prepared by dispersion in ethanol, followed by drop casting onto a copper grid.

Scanning transmission electron microscopy (STEM and EDS mapping: High angle annular dark field scanning transmission electron microscopy (HAADF-STEM), along with the associated EDS spectra and mapping data coupled with corroborating line scans, were acquired using a FEI Talos F200X instrument. Images were generated using an acceleration voltage of 200 kV. For imaging purposes, samples were prepared by initially dispersing in ethanol, followed by drop casting onto 3 mm lacey carbon-coated Au grids to mitigate for any possible signal interference. XPS: To enable samples for use in XPS, powders were dispersed in a small amount of absolute ethanol, followed by drop casting onto a Si wafer (measuring 1 cm × 1 cm). Samples were then placed into the vacuum chamber of a home-built XPS surface analysis system, equipped with a model SPECS Phoibos 100 electron energy analyzer for electron detection. The chamber was evacuated to a base pressure of about 2·10⁻¹⁰ torr. XPS spectra were first collected using an Mg K_{α} X-ray source (with hv = 1250 eV) (model XR 50). In the data analysis, we were able to calibrate the relative positions of the Cu 2p peak and the Ir 4f peak, respectively. The C 1s peak was assigned to a position of 284.5 eV. The Shirley background was then subtracted away, and subsequent curve fitting was performed using the CasaXPS software.

2.5. Experimental Protocol for Ambient Pressure X-ray Photoelectron Spectroscopy (AP-XPS): Reaction with methane.

The reaction of methane with the CuO@IrO₂ samples was investigated within a commercial SPECS AP-XPS chamber, equipped with a PHOIBOS 150 EP MOD-9 analyzer and

a Mg Kα source, located in the Chemistry Division of Brookhaven National Laboratory (BNL).

To maximize the initial concentration of Cu²⁺ and Ir⁴⁺ cations, the samples were drop-cast onto an Al plate and initially oxidized under a 10% O₂/He gas mixture at 1 atm in a flow reactor. Each CuO@IrO₂ sample was subsequently transferred into the AP-XPS chamber and oxidized again at ~ 625 K under 30 mTorr of O₂ for 30 min. This was followed by cooling down to 300 K before 30 mTorr of CH₄ were introduced into the AP-XPS chamber. Data were collected at 300 K under ultra-high vacuum (UHV) conditions, right before the introduction of CH₄. Subsequently, similar experiments were run using 30 mTorr of methane at 300, 350, 400, 450, and 500 K. Our objective was to study the reactivity of the CuO@IrO₂ samples towards the hydrocarbon at low and moderate temperatures to maximize the possibility of transforming CH₄ into stable surface CH_x fragments that can be used in the synthesis of high value chemicals.^{20,22}

For the binding energy calibration, the position of the main line in the Cu Auger LMM spectrum at 300 K (under UHV or 30 mTorr of CH₄) was aligned to 917.7 eV, which denotes the value reported in the literature for bulk CuO.⁴⁰ The initial position of the main line in the Cu Auger LMM collected under 30 mTorr of CH₄ at 350 and 400 K was noted at 917.7 eV, as originally observed.

3. Discussion

3.1. Discussion of Cu@IrO2 Core-Shell Materials

3.1.1. Investigation of Synthetic Alternative Protocols.

To determine the suitability of the microwave methodology for inducing IrO₂ outer shell formation on an inner Cu NW core, we explored the feasibility of other synthetic methods, such as physical sonication, stirring, and refluxing for generating the desired core-shell motif.

3.1.1.1. Physical sonication.

A physical sonication method was utilized to determine if the Cu@IrO₂ motif could be synthesized in this manner. Specifically, the as-prepared Cu NWs were dispersed in an ethanol solution and then sonicated. The Ir salt was then dissolved in absolute ethanol, added in dropwise to the Cu NW solution, and ultimately sonicated for 1 hour. The Cu: Ir ratio was tested using 3 different molar ratios of 1: 1, 2: 1, and 4: 1, respectively (Figure S2A-C respectively). The results highlighted the production of many IrO₂ nanoparticles in the spatial vicinity of the wires with unfortunately very little if any physical attachment onto the wires themselves. As observed from the electron microscopy images, reducing the Ir content by increasing the corresponding Cu: Ir ratio from 1: 1 (Figure S2A) to 4: 1 (Figure S2C) was marginally conducive to the production of the desired product. However, there were major morphological impurities within all samples. The presence of many broken wires coupled with aggregation of IrO₂ nanoparticles suggested that this 'brute force' technique was not necessarily the best means for producing the preferred core@shell structures.

3.1.1.2. *Reflux*.

We also attempted a reflux-based method to synthesized Cu@IrO₂ core@shell nanowires, based upon a previously published procedure for synthesizing PtCu core@shell nanowires.³⁷ Using that procedure, the targeted core@shell nanowires were produced by first dispersing the Cu NWs in octadecene followed by heating to 205 °C under N₂. To introduce in Ir content, an Ir salt solution was added with the resulting solution further heated for 3 hours, followed by washing. The resulting morphology within the solution evinced the presence of aggregated particles clustered around the Cu NWs with very little evident particulate attachment onto the anisotropic wire motif itself (**Figure S3A**).

3.1.1.3. Stirring.

Finally, a stirring method, based on the production of IrO₂ nanoparticles, was tested to analyze its feasibility for core@shell formation.³⁶ Herein, the Ir salt was dissolved in water; the addition of sodium borohydride caused the solution to evolve from a yellow to a blue hue, indicative of IrO₂ formation. A milliliter aliquot of this Ir-containing solution was added to Cu NWs dispersed in absolute ethanol, followed by stirring for 24 hours. The resulting morphology was investigated using TEM (**Figure S3B**). Whereas clusters of IrO₂ nanoparticles did seem to have dispersed onto the external surfaces of the Cu NWs, we also observed a large number of nanoparticulate impurities. Hence, we concluded that this was not a legitimate core@shell motif, because the relative amount of Ir immobilized onto the underlying Cu surface itself was very low. However, the isolated morphology still represented a distinctive improvement with respect to the results of both physical sonication and reflux methods.

Our collective data suggest that the microwave-assisted process we have developed herein represents a reasonable (and perhaps in some cases, the sole reliable) means for producing desirable Cu@IrO₂ core-shell motifs. In fact, we will show that our microwave-based methodology signifies an improvement as compared with the other aforementioned synthesis protocols that have been commonly used in the prior literature.

3.2. Investigation of Variations in Microwave Reaction Parameters

3.2.1. Effect of Irradiation Time

Initial testing was performed using solely the iridium precursor coupled with copper nanowires at an initial 1: 1 molar ratio of Ir: Cu, wherein the Cu NWs were dispersed using sonication followed by addition of the Ir precursor. We then subjected the sample to varying irradiation times from 10 to 30 minutes (**Figure S4A and B** respectively). At the longer reaction

time of 30 minutes, we observed degradation of the nanowires and formation of core@shell nanoparticles (**Figure S4B**). By contrast, a decrease in the reaction time to 10 minutes yielded a more amorphous-like coating on the wires, prior to their subsequent degradation into particles (**Figure S4A**). The chemical composition was confirmed using XRD (**Figure S4Dii**). Observed peaks could be ascribed to Cu and Ir, in line with previously published Cu@Ir core@shell XRD patterns. ²⁴ We should mention that neither oxides nor chlorides were detected in the XRD pattern to any perceptible degree, suggesting that the metals themselves maintained their reduced state. Hence, to systematically alter shell thickness in a controllable manner, we correspondingly varied the molar ratio of Cu: Ir from 1: 1 to 20: 1.

3.2.2. Effect of Method of Precursor Addition

Furthermore, the method of addition of the Ir precursor was also explored. In the above experiments, the Ir precursor was added directly into the solution. However, previous work by our group³⁰ has suggested that enabling a more uniform dispersion of the shell precursor within a separate solution could improve the quality of the resulting core@shell motif. Within our sample, when the Ir precursor was initially dispersed prior to dropwise addition into the Cu NW dispersion, we actually formed CuCl after microwave irradiation (Figure S4 C and Di). This observation could most likely be ascribed to our use of an iridium chloride precursor salt, wherein CuCl impurities can be easily formed. Therefore, direct addition of the Ir precursor into the Cu NW dispersion (as opposed to a stepwise addition process) represents an optimized method for utilizing the Ir precursor. As such, the experiments described in the following sections successively build upon these initial sets of findings. Specifically, we determined that the direct addition of the Ir precursor to the Cu NW solution with a Cu: Ir molar ratio of 20: 1, using an irradiation time of 10 minutes, yielded reasonable, reproducibly pure samples with

which to subsequently probe the discrete effects of other experimental parameters.

3.2.3. Effect of Reducing Agent

As observed in the prior sections, experimental parameters such as irradiation time and method of addition were optimized. To further improve upon the morphology of the core@shell motif, various additives, including reducing agents such as ascorbic acid, were explored, based on analogous findings from previously published studies. Al, 42 Changing the concentration of ascorbic acid represents a direct way of controlling the particle shape, because increasing the amount of reducing agent boosts the corresponding rate of metal ion reduction, which can thereby lead to the growth of more kinetically accessible (or less thermodynamically favorable) particle morphologies. Indeed, ascorbic acid is a milder reducing agent as compared with more reactive analogues, such as sodium borohydride. We have hypothesized that the use of a 'gentler' reducing agent will allow for deliberative control over the outer shell growth circumscribing the underlying inner nanowire structure. In particular, carefully tuning the amount of reducing agent used can yield tangible effects upon both chemical composition and the observed morphology.

In the case of Cu nanostructures, the selection of a milder reducing agent can lead to not only smaller particles but also increased reducibility. For our purposes, a lower particle size is conducive to the formation of a homogeneous shell coverage. Moreover, prior studies also suggested that in combination with PVP as the capping agent, the apparent structural integrity of the product tended to be conserved. Herein, the role of the reducing agent was not only to prevent Cu²⁺ from forming but also to inhibit undesirable side reactions which might have precipitated out copper chloride and copper oxide. That is, it was important that the reducing agent maintain Cu within its reduced state, especially because the Ir precursor was a chloride.

An effective reducing agent, such as ascorbic acid, also could facilitate the reduction of

Ir. However, ascorbic acid itself is insoluble in absolute ethanol, and therefore had to be dispersed in water to ensure some degree of solubility in absolute ethanol. As such, typically, a solution of 0.1 g of ascorbic acid dispersed in 1 mL water was added to 4 mL of absolute ethanol, to which Cu NWs were then inserted, followed by physical sonication until dissolution was achieved. We observed that the use of ascorbic acid enabled a relatively uniform dispersion of Cu NWs within solution. To this overall mixture, IrCl₃ was then added and sonicated for 30 min before 'microwaving' for 10 minutes at 150 °C (**Figure S5A**). SEM images highlighted a relatively non-uniform distribution of species consisting of not only amorphous-like wires/particles (**Figure S5A**) but also wire motifs with particles clearly aggregated onto their external surfaces.

3.2.4. Effect of Capping Agents

Capping agents often act as ligands to form complexes with the original metal precursors and thereby affect their reduction kinetics. ⁴⁴ In addition, capping agents can enable effective shape control to achieve a desired morphology. ⁴³ For example, preferential adsorption of ionic capping agents on specific crystallographic planes normally induces the anisotropic growth of nanocrystals. Previous experiments with nanoscale Cu/Ir-based morphologies have analyzed capping agents, such as hexadecyl ammonium chloride (CTAC) and oleylamine, to create 0D morphologies, such as nanocages and nanocrystals. ^{24, 26} Other commonly used capping agents utilized for creating core@shell nanowires, include oleic acid, hexadecyl ammonium bromide (CTAB), and polyvinyl pyrrolidone (PVP). ³³⁻³⁵ Why were these specific molecules chosen?

These capping agents possess different molecular structures and accordingly, behave dissimilarly in the presence of growing metal-based nanostructures. For example, linear long-chain hydrophobic hydrocarbons, such as oleylamine, oleic acid, and CTAB, often assemble as

an organized array on the particle surface at a tilted angle, whereas unbranched polymers such as PVP physically entangle the nanostructures with partial functional groups attached onto their surfaces. 44 Indeed, surfactants, such as either CTAB or CTAC, produce worm-like micelles and vesicles, in a process driven by the strong hydrophobicity and head group bulkiness of these molecules; these micellar templates are suitable for the synthesis of long nanorods or wires. In addition, because the binding affinities of functional groups within capping agents are dependent on the distinct atom geometries of different facets, oleic acid and oleylamine are significant, due to their carboxylic acid and amine terminal end groups, respectively. 44 Moreover, oleic acid and oleylamine acting in concert have been known to give rise to a different morphology as opposed to use of the individual ligands by themselves.

Therefore, in separate experiments, we ascertained the functionality of various capping agents, such as oleic acid, oleylamine, and CTAB (**Figure S5 B-F**). The surfactants were placed in, after the iridium salt had been added into the copper solution and then sonicated for 15 minutes, prior to microwave irradiation. Multiple capping agents and corresponding capping agent combinations were tested. Unfortunately, many of these capping agents did not successfully generate the targeted composition and morphology, simultaneously.

Illustrative examples are provided as follows. First, the use of oleylamine (0.1 ml) resulted in the formation of not only spindle-like crystals and broken wires but also amorphous species (**Figure S5B**). Second, when oleic acid was utilized (1 mL), we observed some coverage of the wires, but this reagent yielded mostly large particles (**Figure S5C**). Third, a mixture of oleylamine (0.1 mL) and oleic acid (0.1 mL) (**Figure S5D**) appeared to give rise to a relatively uniform coating of IrO₂. However, we concluded that the as-prepared wires were likely coated with an organic layer, postulated to have originated from oleylamine; unfortunately, these wires

were also non-uniform in nature, incorporating not only particles but also amorphous regions. Fourth, ascorbic acid, when used in combination with oleylamine and oleic acid (**Figure S5E**), resulted in the production of large sheets with aggregated particles. Finally, when CTAB was coupled with oleylamine and oleic acid together within a single pot, we detected the formation of a visibly inhomogeneous coating of the wires themselves (**Figure S5F**).

3.2.5. Effect of Varying Ascorbic Acid (AA) – to - PVP Mass Ratio

Our cumulative experiments showed that only polyvinylpyrrolidone, (PVP), in combination with ascorbic acid, produced well-defined Ir coatings around the wires, presumably as a result of increasing the mutual dispersibility of both Cu NWs and the Ir precursor. We postulate that this observation was a function of the unique encapsulation and physical entanglement capability associated with the polymeric PVP 'template', which ensured homodispersity of the nanoparticles in solution and the resulting uniformity of the as-prepared coating. 44 Previous papers have noted a reduction in interfacial bonding between the shell and the core materials in the absence of PVP, indicating that PVP not only acts as a capping agent but also promotes the formation of various nucleation sites for shell formation. 35 By contrast, in the absence of ascorbic acid, the use of PVP (Figure S6) led to core-shell morphologies as well. However, in that latter experiment, there were issues with the isolated sample. Not only was the observed dispersion of the motif perceptibly lower but also irregular clumps of IrO₂ nanoparticles, which were not attached to the underlying Cu NWs, were also apparent.

Hence, in additional runs, the relative amount of reducing agent with PVP was subsequently varied. Initially, the sample was tested with a ratio of 10: 1 AA: PVP ratio by mass with the concentration of Cu: Ir held at a constant 20: 1 molar ratio, as previously discussed. In practice, the ascorbic acid was dissolved into the Cu NW solution, prior to Ir precursor addition,

to which the PVP was later put in and dispersed.

The irradiation time parameter was tested at both 5 minutes and 20 minutes to determine the optimized reaction time for this reaction, as well. Therefore, at a ratio of 10: 1 AA: PVP by mass for 5 minutes (**Figure S7A**), the sample data highlighted a coating around the wire core, which seemed to be etched by the relatively greater amounts of ascorbic acid. Increasing the microwave irradiation time (**Figure S7D**) resulted in the formation of large irregular nanoparticle aggregates. Reducing the AA content by half in the context of a 5: 1 AA: PVP mass ratio (**Figure S7B**) yielded not only little apparent etching of the wire but also a relatively uniform particulate coating of the Cu NW core. Upon increasing the irradiation time to 20 minutes, the resulting shell became amorphous and inhomogeneous (**Figure S7E**). By contrast, a rise in the relative amount of PVP to 40 mg within an AA: PVP mass ratio of 2.5: 1 yielded Ir nanoparticulate aggregation but not necessarily their attachment onto the underlying wire motif (**Figure S7C**). Furthermore, when the microwave irradiation time was extended to 20 minutes under these reaction conditions, the resulting morphology exhibited the presence of large nanoparticle aggregates around the Cu NW, as seen in **Figure S7F**.

Therefore, based on all of these experiments, the optimized reaction conditions used to effectively generate a viable core-shell motif consisted of the use of (i) an AA: PVP mass ratio of 5: 1 coupled with (ii) a molar Cu: Ir ratio of 20: 1, run with (iii) 5 minutes of microwave irradiation, as suggested in **Scheme 1**. Specifically, we hypothesize that the proposed mechanism for core-shell NW formation involves the initial reduction of Ir³⁺ ions using ascorbic acid, followed by their PVP-enabled aggregation and assembly during the microwave process to create the observed external Ir-rich coating on the underlying Cu NWs.

3.3. Structural Characterization of Cu@IrO2 Core@Shell Motifs

3.3.1. XRD and Microscopy Analysis

Based on the optimization of the above reaction parameters, including but not limited to capping agents, irradiation time, the reducing agent-to-capping agent ratio, and the method of Ir precursor addition, the resulting as-synthesized Cu@IrO₂ core@shell motifs were characterized by X-ray diffraction (XRD) and scanning electron microscopy (SEM) methods, as illustrated in **Figure 1**. As presented in the SEM images (**Figure 1A-C**), the core@shell motif gave rise to a homogeneous and uniform particulate IrO₂ shell atop the underlying Cu NW core. Furthermore, the experimental XRD pattern (**Figure 1D**) yielded a diffraction pattern similar to that of Ir and Cu, and consistent with that of previously reported CuIr alloys. ^{24, 25} However, (i) because the outer Ir-containing shell is decidedly smaller by comparison with the inner Cu core and (ii) since the coating itself is predominantly comprised of smaller and presumably amorphous constituent nanoparticles; the lack of any crystalline IrO₂ peaks is not surprising. To complement these results, we embarked upon an additional chemical investigation of the core@shell structure.

3.3.2. XPS Analysis

Chemical characterization of the oxidation states in the as-prepared Cu@IrO₂ motif (created using a 20: 1 molar precursor ratio of Cu: Ir) was achieved using X-ray photoelectron spectroscopy (XPS). Specifically, the full Cu 2p region (**Figure 1F**) was analyzed and consisted of four main features: a dominant $2p_{1/2}$ peak located at 952.5 eV and a less intense $2p_{3/2}$ peak at 932.8 eV, indicative of a Cu⁰/Cu²⁺ mixture, coupled with two strong satellite peaks situated at 941.1 eV and 960.9 eV, consistent with Cu²⁺ formation (**Table S1**). As compared with XRD, XPS is a more surface sensitive technique that mostly detects a copper oxide film on top of the copper substrate that produces the main diffraction lines in Figure 1D. Overall, these XPS data confirm that the Cu NW core is still intact, whereas there is most likely some degree of surface

oxidation, due to exposure to water and O_2 in the air. In addition, the Ir 4f region (**Figure 1E**) exhibits 2 sets of peaks, denoting the presence of Ir^0 and Ir^{4+} (**Table S1**). The elemental Ir^0 peaks can be found at 60.3 eV ($4f_{7/2}$ peak) and 63.3 eV ($4f_{5/2}$ peak), which are likely attributable to the use of ascorbic acid as a reducing agent during synthesis. The Ir^{4+} peaks positioned at 62.0 eV ($4f_{7/2}$) and 65.1 eV ($4f_{5/2}$) can most likely be ascribed to surface oxidation of the Ir layer, due to the use of ethanol as the solvent with residual water. These data corroborate the observed molar ratio of Ir^0 : Ir^{4+} to be ~ 3.8 : 1. This finding is consistent with the proposed core-shell formation mechanism, highlighted in **Scheme 1**, in which the presence of ascorbic acid not only reduces the Ir ions but also maintains the Cu NWs within their reduced state.

3.3.3. Effect of the Ir Precursor Concentration on Shell Size

The Cu@IrO₂ core@shell motif, formed using a 20: 1 molar ratio, was further characterized by HRTEM analysis (**Figure 2 C, G, K**). The outer particulate shell is clearly observed, circumscribing the inner surface of the core@shell motif (**Figure 2C**), which is further highlighted by the red bracket denoting the Cu 'core' and the green bracket designating the IrO₂ 'shell' in **Figure 2G**. The 'shell' size was determined to be 5.9 ± 1.3 nm (**Table S2**). The HRTEM diffraction analysis highlights the expected d_{101} plane of IrO₂ with the associated lattice spacing of 2.60 Å, as shown in **Figure 2K**.

To determine if the shell size itself was a tunable parameter, the dimension of IrO₂ shell was systematically varied by altering the molar Cu: Ir ratio, while maintaining the corresponding AA: PVP mass ratio. In particular, by increasing Ir content (or conversely successively decreasing the Cu: Ir ratio from 20: 1, 15: 1, to 10: 1, in practice) while proportionately raising the relative amounts of PVP and AA within the overall reaction medium, the resulting IrO₂ shell was observed to have correspondingly augmented in size (**Table S2** and **Figure 2 A, E, I** for the

10: 1 sample and **Figure 2 B, F, J** for the 15:1 sample). The Cu 'core' and IrO₂ 'shell' are denoted by the red bracket and green bracket, respectively, as presented in **Figure 2E**. Upon systematically increasing Ir content with samples incorporating ever decreasing Cu: Ir molar ratios of 20: 1, 15: 1, and 10: 1, respectively, we were able to demonstrate that the shell size could be reliably increased in size from \sim 6 nm, onwards to 8.2 ± 2.4 nm, and ultimately 9.5 ± 2.7 nm, respectively (**Table S2**). The presence of IrO₂ (101) within the HRTEM image was confirmed by indexing the associated lattice fringes; measured *d*-spacings at \sim 0.262 nm and \sim 0.264 nm respectively, were consistent with literature.

The boost in the observed d-spacing with increasing shell size has been previously reported in prior studies. ³⁰ Specifically, to decrease shell size, the Cu: Ir molar ratio could be increased from 20: 1 to 25: 1 by raising the relative amount of Cu NWs in solution, while maintaining the AA: PVP mass ratio (**Figure 2 D, H, L** and Table S2). Specifically, as shown in **Figure 2H** with the shell and core designated by the green and red brackets respectively, we observed that the shell size could be decreased from 6 nm to 3.4 nm \pm 1.4 nm across this experimental range. Furthermore, the shell size diminution correlated with a decrease in the d spacing of the IrO₂ (101) signal, computed to be \sim 0.254 nm, a result consistent with prior literature. ³⁰ Overall, based on an analysis of these collective data, we were able to show that the relative dimensions of the core and shell within our as-prepared Cu@IrO₂ core@shell motifs could be successfully manipulated by deliberatively controlling the molar ratio of Cu: Ir, in conjunction with the relative amounts of capping agent (PVP) and reducing agent (AA) in the guise of a constant AA: PVP mass ratio.

A plot of the Cu: Ir molar ratios versus the radius of the observed shell is presented in **Figure 3**. While highlighting a proportionate correlation, it is also indicative of a reasonably

robust linear relationship ($R^2 = 0.984$), by contrast with previously reported literature, using a similar fabrication protocol.³⁰ Such discrepancies are most likely a result of differences in the associated synthetic process parameters, such as the choice of precursor, surfactant, and reducing agent. Specifically, in the microwave-assisted synthesis reported herein, control over the shell thickness is dictated to a large extent by the precise amounts of metal-based precursors used to generate the core and shell, respectively.

Upon further increasing the relative amounts of Ir content (all else being equal) through the creation of samples incorporating 5: 1 and 7.5: 1 Cu: Ir molar ratios, we observed an increased formation of discrete IrO₂ nanoparticles. This finding was supported by data from SEM images presented in **Figure S8A and B**, associated with the 5: 1 and 7.5: 1 Cu: Ir samples, respectively. Furthermore, TEM analysis of the 7.5: 1 sample suggested a relatively poorly formed shell. The exterior surface appeared to be roughened and with little to no shell uniformity; in fact, we observed predominantly clusters of discrete IrO₂ nanoparticles immobilized onto these Cu NWs (**Figure S9**). Overall, these results collectively imply that there is likely an upper limit threshold on the magnitude of the size of a relatively homogeneous, uniform shell that is realistically achievable.

Furthermore, relevant HRTEM-EDS data mapping were used to confirm the extent of a homogeneous Ir distribution within these samples (**Figure 4**). As seen from the data in the Figure, all of the samples probed ((A) 10: 1, (B) 15: 1, (C) 20: 1, and (D) 25: 1) yielded a reasonably homogeneous dispersion of Cu (red), Ir (green), and O (blue) elements throughout the entirety of the specimens analyzed. It was observed with HAADF that Ir was indeed present throughout the shell in the guise of relatively small 1-2 nm particles, which, due to the extremely low quantities available within the structure, resulted in a significantly reduced Ir signal. This

assertion is also confirmed by the lack of any IrO₂ detectable in the XRD pattern. Nevertheless, these collective findings are consistent with the existence of an outer IrO₂ shell circumscribing an inner Cu NW, despite variations in the actual magnitude of the shell.

4. Methane Activation

4.1. Overview of Structural Integrity

In order to prepare the Cu@IrO₂ materials for methane activation, the as-prepared samples were initially annealed under an oxygen-rich atmosphere at ~ 625 K not only to remove any remaining contaminant carbon but also to maximize the amount of Cu²⁺ and Ir⁴⁺ cations present on the surfaces of the core@shell motif. As suggested by the associated TEM (**Figure 5A**) and HRTEM-EDS images (**Figure 5C**), the core@shell architecture remained intact after this oxidation processing treatment. Significantly, as presented in **Figure 5C**, we observed not only the homogeneous elemental dispersion of O and Ir on the outer sample surface but also the preservation of the inner Cu core. Indeed, there was no apparent damage to the overall nanowire morphology, associated with the oxidative treatment itself, implying that the tested catalytic material maintained good structural stability under thermally activated conditions.

We also evaluated the structural integrity of the core@shell motif after the methane activation process described in the next section, wherein the Cu@IrO₂ materials were exposed to the hydrocarbon up to a temperature of 500 K. Again, as demonstrated in **Figure 5B**, the TEM images (**Figure 5B**) confirm that the nanowire core@shell architecture was conserved after the methane activation reaction. HRTEM-EDS (**Figure 5D**) data further corroborate this idea of a reasonably uniform dispersion of O and Ir elements, surrounding an internal Cu core, superimposed upon the underlying anisotropic nanowire motif. Based on this analysis, we can

conclude that the Cu@IrO₂ core@shell architecture is sufficiently robust to survive not only high temperature oxidation but also methane activation conditions.

4.2. Chemical State Before and After Reaction with Methane: Analysis of AP-XPS Spectra 4.2.1. The oxidized Cu@IrO2 materials

The samples that produced the TEM and HRTEM-EDS images in **Figure 5A** and **5C** exhibited Cu 2p, Cu LMM, and Ir 4f spectra typical of Cu²⁺ and Ir⁴⁺ cations. In general, the XPS data were consistent with a configuration in which an external shell of IrO₂ coated an inner core, comprised of a thin CuO film covering the copper NWs. The O 1s data pointed to interesting properties for the individual oxides and possible IrO₂ \leftrightarrow CuO interactions (**Figure 6**). O 1s XPS spectra were acquired for not only the 10: 1 (green) and 25: 1 (blue) Cu@IrO₂ core@shell motifs but also bulk CuO (black) and IrO₂ (purple) standards. Unfunctionalized Cu NW control samples (red) exhibited an O 1s spectrum which is very similar to that of bulk copper oxide (CuO), implying that the nanowires were successfully oxidized in the pre-treatment process with O₂.

Upon addition of the IrO₂ to the Cu NWs, the resulting core@shell material was characterized by an increase in the signal around 531.4 eV, a peak location which is close to that of super-stoichiometric oxygen in CuO_x (1<x<2).⁴⁶ Otherwise, it is indicative of very intense features previously observed for some oxides of iridium.⁴⁷⁻⁴⁹ This distinctive 531.4 eV signal is exhibited far more strongly in the 10: 1 Cu@IrO₂ system (green), especially as compared with the corresponding spectrum for the 25: 1 Cu@IrO₂ (blue) material. In the latter case, the signal is weaker but still clearly observable and is not surprising, considering that the intensity appears to correlate with a decrease in iridium content.

We note that the observed line shape of the O 1s spectrum in the 10: 1 Cu@IrO₂ system could not be obtained by a simple linear combination of the corresponding spectra derived from

its bulk constituent CuO and IrO₂ units. Instead, the structure of the 10: 1 Cu@IrO₂ sample could be explained by the existence of strong bonding interactions between the discrete CuO and IrO₂ components. By contrast, with the 25: 1 Cu@IrO₂ system, it is possible that the surface oxygen atoms are localized within a shell of iridium oxide, which may either possess an atypical metal oxide structure or incorporate a large number of lattice defects.⁴⁷⁻⁴⁹

In both of the Cu@IrO₂ samples, it is conceivable that we have generated a mixture of Cu²⁺ and Ir⁴⁺ species, which would induce the formation of oxygen species within Ir-O-Cu arrays, as had been previously observed with an earlier Cu@IrO₂ core-shell study.²⁰ What is evident is that the O 1s spectra collectively show that the CuO@IrO₂ systems are not necessarily the result of a simple superposition of signals attributable to bulk IrO₂ onto either a CuO or Cu nanowire core. Rather, the scenario is likely to be more nuanced and complex, a finding which is consistent with prior literature on analogous systems. Nevertheless, the Cu@IrO₂ core shell structures seem to exhibit special, atypical electronic properties, associated with the oxygen centers and ascribable to the simultaneous presence of a mixture of these two different metal oxides, all of which can lead to the observation of an enhanced catalytic behavior.

4.2.2. Reaction with Methane: Changes in the Cu and Ir Oxidation States

4.2.2.1. Analysis of the Cu LMM region

AP-XPS, a surface-sensitive technique, was used to track the chemical evolution of the core@shell samples as they underwent changes associated with methane activation. To establish the oxidation state of copper, complementary Cu Auger LMM (**Figure 7**) and Cu $2p_{3/2}$ XPS (**Figure 8**) signals were examined. The line-shape of the Cu Auger LMM region is extremely sensitive to changes in the oxidation state of copper, as it evolves from Cu⁰ to Cu¹⁺ and Cu^{2+,40} Furthermore, as shown in **Figure 7**, at 300 K after the oxidation treatment (red), all of the

samples that contain copper show the same Cu Auger LMM line shape with a main peak located at 917.7 eV, which represents a typical, identifying 'fingerprint' signal for CuO.⁴⁰ Upon exposure to methane, at 500 K (**Figure 7, yellow**), there is a change in the observed line-shape with features appearing around 916.8 eV, all of which indicate that the CuO has been partially reduced to Cu₂O by reaction with the hydrocarbon.

4.2.2.2. Analysis of the Cu 2p region

The Cu $2p_{3/2}$ region associated with the XPS spectra (**Figure 8**) was similarly investigated. Specifically, the appearance of strong satellite peaks at 940-945 eV confirms the presence of CuO in all of the analyzed systems, and the data are consistent with the findings from the O 1s region, as described in the previous section. At 500 K within the Cu $2p_{3/2}$ spectra (**Figure 8, yellow**), the position of the main peak exhibits a peak shift toward a lower binding energy value, coupled with a corresponding decrease in the intensity of the satellite signal.

Therefore, as noted in both the Cu Auger LMM (**Figure 7**) and Cu $2p_{3/2}$ regions (**Figure 8**), apparent changes to the copper oxidation state ($Cu^{2+} \rightarrow Cu^{1+}$) are observed, after exposing all of the samples to methane at temperatures above 400 K (green traces). By 500 K (yellow), it is evident that a significant part of the copper oxide has been reduced by the reaction with methane. On the surfaces of these systems, the oxygen is probably removed by reaction with either H or C adatoms, produced by the dissociation of methane. In the corresponding C 1s XPS spectra (**Figure S10**), we found that exposure to the hydrocarbon led to the deposition of CH_x fragments on all of the samples at 300-500 K. It is worth highlighting that all of the CuOcontaining systems appear to show similar behaviorial trends in the presence of methane (**Figures 7 and 8**).

4.2.2. Analysis of Ir 4f regions

Changes in the oxidation state of the IrO₂ shell were likewise monitored, in order to track the corresponding variations in the Ir 4f core levels (**Figure 9**). Because of the low intensity associated with the Ir 4f signal exhibited by the 25: 1 Cu@IrO₂ sample, which can most likely ascribed to the low iridium content, the analysis will focus on the 10: 1 Cu@IrO₂ sample (**Figure 9A**). Furthermore, the 10: 1 Cu@IrO₂ sample evinced interesting electronic properties, as noted with the O data in **Figure 6**. Bulk IrO₂ was also tested by means of comparison (**Figure 9B**), with the position of the $4f_{5/2}$ peak appearing at 62.1 eV (**Figure 9B, red**). The binding energy values in the range of 61.9 to 62.7 eV have been reported for Ir⁴⁺, with the variation likely due to the effects related to the oxide crystal structure and the particle size. $^{47-50}$ We have found that the oxidized 10: 1 Cu@IrO₂ sample displays both a spectral line-shape and a $4f_{5/2}$ peak position, which are noticeably different from those of the bulk IrO₂, even though both systems contain Ir⁴⁺ species (**Figure 9A, black**). $^{47-50}$

When subjected to a methane atmosphere at temperatures above 400 K (green), there were likely chemical changes, induced in both the iridium and copper oxide constituent components of the core-shell NW architecture. As an example, such chemically-generated modifications were evident within the 10: 1 Cu@IrO₂ sample (Figure 7 and 8). Indeed, at 500 K (Figure 9, yellow), there was a reduction in the amount of iridium oxide present, with a minor binding energy shift towards 60.8 eV at which stage, Ir⁰ appears. In the case of bulk IrO₂ (Figure 9B, yellow), the reduction of the oxide by methane is more difficult to observe, but when comparing the spectra obtained at 300 (Figure 9B, red) and 500 K (Figure 9B, yellow) under CH₄, respectively, there is an evident reduction in the size of the 'valley' (or gap) between the Ir 4f_{3/2} and Ir 4f_{5/2} peaks, implying the existence of a discernible reactivity with methane. The data presented in Figure 9 suggest that the IrO₂ shell enables a higher activity towards methane as

compared with that of bulk IrO₂. This finding could be a consequence of either the presence of defects or lattice imperfections within the IrO₂ shell, which likely account for the distinctive O 1s line-shape for the 10: 1 Cu@IrO₂ sample in **Figure 6.**

Therefore, based on the AP-XPS analysis, it can be deduced that the Cu@IrO₂ core-shell structures are active for the activation of methane at relatively low temperatures. At 300 K, the cleavage of C-H bonds in the adsorbate leads to the deposition of CH_x fragments on the Cu@IrO₂ samples (**Figure S10**), but there is no significant change in the oxidation states of copper and iridium. By 500 K (**Figure 7 and Figure 8, yellow**), the copper oxide constituent appears to undergo a massive reduction process, whereas there is a comparatively minor reduction of the iridium oxide component (**Figure 9A, yellow**). This is a key finding for the applicability of these core-shell structures for methane activation.²⁰ In principle, our results show that the copper oxide-iridium oxide interface present within these core-shell structures is not only stable but also chemically active under relatively mild reaction conditions. The CH_x fragments deposited on this interface can be the starting point for the conversion of methane to high value chemicals through reaction processes in which the presence of copper alone is insufficient to observe catalytic activity.^{20,21} By contrast, within our core-shell structures, the synergistic combination of *both* copper and iridium opens the door for a favorable catalytic performance.²⁰

5. Future work and Conclusions

A core@shell motif of Cu@IrO₂ was successfully synthesized using a novel microwave irradiation technique. Experimental parameters, such as (i) irradiation time, (ii) the method of Ir precursor addition, (iii) capping agent, and (iv) reducing agent, were systematically explored and optimized using a novel microwave method. In particular, the most effective reducing agent and

capping agent were found to be ascorbic acid and polyvinylpyrrolidone, respectively. We determined the most effective AA: PVP mass ratio to be 5: 1, in the presence of a 20:1 Cu: Ir molar precursor ratio. The reaction worked best at 5 minutes at an irradiation temperature of 95 °C. The chemical composition was assessed using a combination of XRD, HRTEM-EDS, and XPS data, respectively. Furthermore, the shell dimension over a range spanning from 3.5 to 10 nm could be primarily altered by deliberative changes to the Cu: Ir molar ratio.

The as-prepared core@shell structures were found to be stable and capable of activating methane at temperatures of 300 to 500 K, regardless of shell size. At 300 K, CH_x fragments were deposited on the CuO-IrO₂ interfaces and significant reduction of the metal cations occurred at 400-500 K. Our data highlighted the distinctly higher activities measured for methane activation as compared with the corresponding bulk, denoting observations consistent with our extensive AP-XPS analysis. These results strongly suggest that the as-synthesized Cu@IrO₂ systems represent a viable potential catalyst for the conversion of relatively simple hydrocarbons to higher value chemicals under moderate temperatures and accessible reaction conditions.

6. Supporting Information: Characterization data obtained on (i) Cu NW controls; (ii) samples prepared by sonication, refluxing, and stirring methods; as well as (iii) samples generated by varying reaction parameters, such as but not limited to irradiation times, the method of precursor addition, capping agents, and molar precursor ratios; in addition to XPS spectra collected for Cu@IrO₂ samples in the presence of methane, coupled with quantitative XPS and HRTEM data acquired for these core@shell architectures.

7. Acknowledgements

This material is based on work performed in SSW's laboratory, supported by the U.S. National Science Foundation under Grant No. CHE-1807640. Structural characterization

experiments (TEM and SEM) for this manuscript were performed in part at the Center for Functional Nanomaterials, located at Brookhaven National Laboratory, which is supported by the U.S. Department of Energy under Contract No. DE-SC0012704. The catalytic activity measurements were supported by the Division of Chemical Science, Geosciences, and Bioscience of the Office of Basic Energy Sciences at the U.S. Department of Energy (DOE) under Contract No DE-SC0012704.

References -

- 1. Casanovas, A.; Roig, M.; de Leitenburg, C.; Trovarelli, A.; Llorca, J., Ethanol steam reforming and water gas shift over Co/ZnO catalytic honeycombs doped with Fe, Ni, Cu, Cr and Na. *Int. J. Hydrogen Energy* **2010**, 35, (15), 7690-7698.
- 2. Zhang, B.; Tang, X.; Li, Y.; Cai, W.; Xu, Y.; Shen, W., Steam reforming of bio-ethanol for the production of hydrogen over ceria-supported Co, Ir and Ni catalysts. *Catal. Commun.* **2006,** 7, (6), 367-372.
- 3. Qiao, D.; Lu, G.; Guo, Y.; Wang, Y.; Guo, Y., Effect of water vapor on the CO and CH₄ catalytic oxidation over CeO₂-MO_x (M=Cu, Mn, Fe, Co, and Ni) mixed oxide. *J Rare Earth* **2010,** 28, (5), 742-746.
- 4. Lytkina, A. A.; Zhilyaeva, N. A.; Ermilova, M. M.; Orekhova, N. V.; Yaroslavtsev, A. B., Influence of the support structure and composition of Ni–Cu-based catalysts on hydrogen production by methanol steam reforming. *Int. J. Hydrogen Energy* **2015**, 40, (31), 9677-9684.
- 5. Pérez-Hernández, R.; Gutiérrez-Martínez, A.; Espinosa-Pesqueira, M. E.; Estanislao, M. L.; Palacios, J., Effect of the bimetallic Ni/Cu loading on the ZrO₂ support for H₂ production in the autothermal steam reforming of methanol. *Catal. Today* **2015**, 250, 166-172.
- 6. Geng, H.; Yang, Z.; Ran, J.; Zhang, L.; Yan, Y.; Guo, M., Low-concentration methane combustion over a Cu/γ -Al₂O₃ catalyst: effects of water. *RSC Adv.* **2015**, 5, (24), 18915-18921.
- 7. Bernardo, C. A.; Alstrup, I.; Rostrup-Nielsen, J. R., Carbon deposition and methane steam reforming on silica-supported Ni-Cu catalysts. *J. Catal.* **1985**, 96, (2), 517-534.
- 8. Park, M. B.; Park, E. D.; Ahn, W.-S., Recent Progress in Direct Conversion of Methane to Methanol Over Copper-Exchanged Zeolites. *Front. Chem.* **2019**, 7, (514), 514-514.
- 9. Huang, T.-J.; Yu, T.-C.; Jhao, S.-Y., Weighting Variation of Water-Gas Shift in Steam Reforming of Methane over Supported Ni and Ni-Cu Catalysts. *Ind. Eng. Chem. Res.* **2006**, 45, (1), 150-156.
- 10. Djaidja, A.; Kiennemann, A.; Barama, A., Effect of Fe or Cu addition on Ni/Mg-Al and Ni/MgO catalysts in the steam-reforming of methane. *Stud. Surf. Sci. Catal.* **2006,** 162, 945-952.
- 11. Geng, H.; Yang, Z.; Zhang, L.; Ran, J.; Chen, Y., Experimental and kinetic study of methane combustion with water over copper catalyst at low-temperature. *Energy Convers. Manage.* **2015**, 103, 244-250.
- 12. Ali, S.; Al-Marri, M. J.; Al-Jaber, A. S.; Abdelmoneim, A. G.; Khader, M. M., Synthesis, characterization and performance of Pd-based core-shell methane oxidation nano-catalysts. *J Nat. Gas. Sci. Eng.* **2018**, 55, 625-633.
- 13. Wang, F.; Xu, L.; Shi, W., Syngas production from CO₂ reforming with methane over core-shell Ni@SiO₂ catalysts. *J. CO2 Util.* **2016**, 16, 318-327.
- 14. Das, S.; Pérez-Ramírez, J.; Gong, J.; Dewangan, N.; Hidajat, K.; Gates, B. C.; Kawi, S., Core–Shell Structured Catalysts for Thermocatalytic, Photocatalytic, and Electrocatalytic Conversion of CO₂. *Chem. Soc. Rev.* **2020**, 49, 2937-3004.
- 15. Ilsemann, J.; Straß-Eifert, A.; Friedland, J.; Kiewidt, L.; Thöming, J.; Bäumer, M.; Güttel, R., Cobalt@Silica Core-Shell Catalysts for Hydrogenation of CO/CO₂ Mixtures to Methane. *ChemCatChem* **2019**, 11, (19), 4884-4893.
- 16. Wu, T.; Cai, W.; Zhang, P.; Song, X.; Gao, L., Cu–Ni@SiO₂ alloy nanocomposites for methane dry reforming catalysis. *RSC Adv.* **2013**, 3, (46), 23976-23979.

- 17. Nguyen, H. M.; Pham, G. H.; Tade, M.; Phan, C.; Vagnoni, R.; Liu, S., Microwave-Assisted Dry and Bi-reforming of Methane over M–Mo/TiO₂ (M = Co, Cu) Bimetallic Catalysts. *Energy & Fuels* **2020**, 34, (6), 7284-7294.
- 18. Lopez, J. S.; Dagle, V. L.; Deshmane, C. A.; Kovarik, L.; Wegeng, R. S.; Dagle, R. A., Methane and Ethane Steam Reforming over MgAl₂O₄-Supported Rh and Ir Catalysts: Catalytic Implications for Natural Gas Reforming Application. *Catalysts* **2019**, *9*, 801 / 1-19.
- 19. Fung, V.; Hu, G.; Tao, F.; Jiang, D.-E, Methane Chemisorption on Oxide-Supported Pt Single Atom. *ChemPhysChem* **2019**, 20, (17), 2217-2220.
- 20. Yang, L.; Huang, J.; Ma, R.; You, R.; Zeng, H.; Rui, Z., Metal–Organic Framework-Derived IrO₂/CuO Catalyst for Selective Oxidation of Methane to Methanol. *ACS Energy Letters* **2019**, 4, (12), 2945-2951.
- 21. Zhang, F.; Yao, S.; Liu, Z.; Gutiérrez, R. A.; Vovchok, D.; Cen, J.; Xu, W.; Ramírez, P. J.; Kim, T.; Senanayake, S. D.; Rodriguez, J. A., Reaction of Methane with MOx/CeO₂ (M = Fe, Ni, and Cu) Catalysts: In Situ Studies with Time-Resolved X-ray Diffraction. *J. Phys. Chem. C* **2018**, 122, (50), 28739-28747.
- 22. Liang, Z.; Li, T.; Kim, M.; Asthagiri, A.; Weaver, J. F., Low-temperature activation of methane on the IrO₂ (110) surface. *Science* **2017**, 356, (6335), 299-299.
- 23. Liu, Y.-C.; Yeh, C.-H.; Lo, Y.-F.; Nachimuthu, S.; Lin, S. D.; Jiang, J.-C., In situ spectroscopic and theoretical investigation of methane activation on IrO₂ nanoparticles: Role of Ir oxidation state on C-H activation. *J. Catal.* **2020**, 385, 265-273.
- 24. Yoon, D.; Bang, S.; Park, J.; Kim, J.; Baik, H.; Yang, H.; Lee, K., One pot synthesis of octahedral {111} CuIr gradient alloy nanocrystals with a Cu-rich core and an Ir-rich surface and their usage as efficient water splitting catalyst. *CrystEngComm* **2015**, 17, (36), 6843-6847.
- 25. Kwon, T.; Hwang, H.; Sa, Y. J.; Park, J.; Baik, H.; Joo, S. H.; Lee, K., Cobalt Assisted Synthesis of IrCu Hollow Octahedral Nanocages as Highly Active Electrocatalysts toward Oxygen Evolution Reaction. *Adv. Funct. Mater.* **2017**, 27, (7), 1604688-1604688.
- 26. Wang, C.; Sui, Y.; Xiao, G.; Yang, X.; Wei, Y.; Zou, G.; Zou, B., Synthesis of Cu–Ir nanocages with enhanced electrocatalytic activity for the oxygen evolution reaction. *J. Mater. Chem. A* **2015**, 3, (39), 19669-19673.
- Wang, C.; Moghaddam, R. B.; Bergens, S. H., Active, Simple Iridium—Copper Hydrous Oxide Electrocatalysts for Water Oxidation. *J. Phys. Chem. C* **2017**, 121, (10), 5480-5486.
- 28. Tian, Y.; Liu, X.; Cao, X.; Zhang, D.; Xiao, S.; Li, X.; Le, Z.; Li, X.; Li, H., Microwave-assisted synthesis of 1T MoS₂/Cu nanowires with enhanced capacity and stability as anode for LIBs. *Chem. Eng. J.* **2019**, 374, 429-436.
- 29. Bilecka, I.; Niederberger, M., Microwave Chemistry for Inorganic Nanomaterials Synthesis. *Nanoscale* **2010**, **2**, (8), 1358-1358.
- 30. Salvatore, K. L.; Deng, K.; Yue, S.; McGuire, S. C.; Rodriguez, J. A.; Wong, S. S., Optimized Microwave-Based Synthesis of Thermally Stable Inverse Catalytic Core—shell Motifs for CO₂ Hydrogenation. *ACS Appl. Mater. Interfaces* **2020**, 12, (29), 32591-32603.
- 31. Liu, D.; Wu, B.; Mubeen, S.; Ding, K.; Zeng, H.; Chuong, T. T.; Moskovits, M.; Stucky, G. D., Microwave-Assisted Synthesis of Ultrastable Cu@TiO₂ Core-Shell Nanowires with Tunable Diameters via a Redox-Hydrolysis Synergetic Process. *ChemNanoMat* **2018**, 4, (9), 914-918.
- 32. Pei, J.; Mao, J.; Liang, X.; Chen, C.; Peng, Q.; Wang, D.; Li, Y., Ir–Cu nanoframes: one-pot synthesis and efficient electrocatalysts for oxygen evolution reaction. *Chem. Commun.* **2016**, 52, (19), 3793-3796.

- 33. Lee, Y.; Kim, J.; Yun, D. S.; Nam, Y. S.; Shao-Horn, Y.; Belcher, A. M., Virustemplated Au and Au–Pt core–shell nanowires and their electrocatalytic activities for fuel cell applications. *Energy Environ. Sci.* **2012**, *5*, (8), 8328-8334.
- 34. Niu, Z.; Chen, S.; Yu, Y.; Lei, T.; Dehestani, A.; Schierle-Arndt, K.; Yang, P., Morphology-controlled transformation of Cu@Au core-shell nanowires into thermally stable Cu₃Au intermetallic nanowires. *Nano Res.* **2020**, 13, (9), 2564-2569.
- 35. Ma, J.; Wang, K.; Zhan, M., Growth Mechanism and Electrical and Magnetic Properties of Ag–Fe₃O₄ Core–Shell Nanowires. *ACS Appl. Mater. Interfaces* **2015**, 7, (29), 16027-16039.
- 36. Chakrapani, K.; Sampath, S., The dual role of borohydride depending on reaction temperature: synthesis of iridium and iridium oxide. *Chem. Commun.* **2015**, 51, (47), 9690-9693.
- 37. Hong, W.; Wang, J.; Wang, E., Facile synthesis of PtCu nanowires with enhanced electrocatalytic activity. *Nano Res.* **2015**, 8, (7), 2308-2316.
- 38. Jae-min, C.; Park, S.-H.; Ryu, B.-K., Synthesis of Cu–SiO₂ Core–Shell Using Ultrasonic Waves and Its Antibacterial Activity. *Glass Phys. Chem* **2019**, 45, (6), 518-524.
- 39. Qian, F.; Lan, P. C.; Olson, T.; Zhu, C.; Duoss, E. B.; Spadaccini, C. M.; Han, T. Y.-J., Multiphase Separation of Copper Nanowires. *Chem. Commun.* **2016**, 52, (78), 11627-11630.
- 40. Biesinger, M. C., Advanced analysis of copper X-ray photoelectron spectra. *Surf. Interface Anal.* **2017**, 49, (13), 1325-1334.
- 41. Chu, X.-Z.; Cheng, Z.-P.; Zhao, Y.-J.; Xu, J.-M.; Li, M.-S.; Hu, L.; Zhou, S.-Y.; Wu, F.-Y.; Lee, C.-H., Morphology control of mesoporous Cu₂O by reductants and its photocatalytic activity. *Ceram. Int.* **2017**, 43, (11), 8222-8229.
- 42. Ma, L.; Liang, S.; Liu, X.-L.; Yang, D.-J.; Zhou, L.; Wang, Q.-Q., Synthesis of Dumbbell-Like Gold–Metal Sulfide Core–Shell Nanorods with Largely Enhanced Transverse Plasmon Resonance in Visible Region and Efficiently Improved Photocatalytic Activity. *Adv. Funct. Mater.* **2015**, 25, (6), 898-904.
- 43. Bakshi, M. S., How Surfactants Control Crystal Growth of Nanomaterials. *Cryst. Growth Des.* **2016**, 16, (2), 1104-1133.
- 44. Niu, Z.; Li, Y., Removal and Utilization of Capping Agents in Nanocatalysis. *Chem. Mater.* **2014**, 26, (1), 72-83.
- 45. Liu, X.; Wang, X.; Han, Q.; Qi, C.; Wang, C.; Yang, R., Facile synthesis of IrO₂/rGO nanocomposites with high peroxidase-like activity for sensitive colorimetric detection of low weight biothiols. *Talanta* **2019**, 203, 227-234.
- 46. Stadnichenko, A. I.; Sorokin, A. M.; Boronin, A. I., XPS, UPS, and STM studies of nanostructured CuO films. *J. Struct. Chem.* **2008**, 49, (2), 341-347.
- 47. Horng, R. H.; Wuu, D. S.; Wu, L. H.; Lee, M. K., Formation process and material properties of reactive sputtered IrO₂ thin films. *Thin Solid Films* **2000**, 373, (1), 231-234.
- 48. Bozack, M. J., Sputter-Induced Modifications of IrO₂ During XPS Measurements. *Surf. Sci. Spectra* **1993**, 2, (2), 123-127.
- 49. Novotny, Z.; Tobler, B.; Artiglia, L.; Fischer, M.; Schreck, M.; Raabe, J.; Osterwalder, J., Kinetics of the Thermal Oxidation of Ir(100) toward IrO₂ Studied by Ambient-Pressure X-ray Photoelectron Spectroscopy. *J. Phys. Chem. Lett.* **2020**, 11, (9), 3601-3607.
- 50. Pfeifer, V.; Jones, T. E.; Velasco Vélez, J. J.; Massué, C.; Arrigo, R.; Teschner, D.; Girgsdies, F.; Scherzer, M.; Greiner, M. T.; Allan, J.; Hashagen, M.; Weinberg, G.; Piccinin, S.; Hävecker, M.; Knop-Gericke, A.; Schlögl, R., The electronic structure of iridium and its oxides. *Surf. Interface Anal.* **2016**, 48, (5), 261-273.

Figure Captions

Figure 1. (A-C) SEM images, (D) XRD pattern, and XPS spectra of the (E) Ir 4*f* and (F) Cu 2*p* regions of Cu@IrO₂ core@shell architectures, created using a 20: 1 Cu: Ir molar ratio coupled with a 5: 1 AA: PVP mass ratio, along with a microwave irradiation time of 5 minutes.

Figure 2. Effect of Varying Cu: Ir Molar Precursor Ratios. Altering shell size by changing the molar ratio between Cu: Ir to be (A, E, G) 15: 1; (B, F, J),10: 1; (C, G, K) 20: 1; and (D, H, L) 25: 1, as highlighted by corresponding HRTEM images. IrO₂ (101) facet is indexed in (I-L)). **Figure 3.** Plot of Cu: Ir molar precursor ratios vs. isolated shell thicknesses. The linear fit (in red) is associated with an R² value of 0.984.

Figure 4. HRTEM-EDS mapping data of the (A) 10:1, (B) 15: 1, (C) 20: 1, and (D) 25: 1 Cu@IrO₂ core@shell systems. From left to right, we observe signals attributed to Cu (red), O (blue), and Ir (green), along with the associated overlay (second column from right). HAADF images (far right column) highlight the particulate nature of the Ir coating.

Figure 5. Probing Catalyst Morphology and Composition, (A) Prior to and (B) Subsequent to the Methane Activation Process at 500 K. TEM images of the 10: 1 sample, (A) post oxidation treatment / pre-methane activation as well as (B) after the methane activation reaction itself. Corresponding HRTEM-EDS images associated with (C) the post-oxidation treatment / pre-methane activation and (D) post-methane activation reaction, respectively, of a 10: 1 Cu: Ir molar ratio Cu@IrO₂ core@shell motif. TEM images (main and inset) evince no apparent destruction of the structural integrity of the core@shell structure in either case. Moreover, HRTEM-EDS images highlight the relatively uniform elemental dispersion of Cu, O, and Ir, along with the resulting overlay, regardless of treatment or reaction process.

Figure 6. O 1s XPS spectra for 10: 1 Cu@IrO₂ (green), 25: 1 Cu@IrO₂ (blue), Cu NWs (red), commercial CuO (black), and commercial IrO₂ (purple) samples, respectively. All the spectra were collected at 300 K under UHV conditions. The Cu NWs and the Cu@IrO₂ samples were treated in O₂ at \sim 625 K before collecting the reported O 1s spectra.

Figure 7. AP-XPS data associated with the Cu Auger LMM region of several samples: (a) 10: 1 Cu@IrO₂, (b) 25: 1 Cu@IrO₂, (c) Cu NWs, and (d) commercial CuO, respectively. The spectra were collected stepwise at 300 K under UHV (black), and at 300 (red), 350 (blue), 400 (green), 450 (purple), and 500 K (yellow) under 30 mTorr of CH₄. The Cu NWs and the Cu@IrO₂ samples were treated in O₂ at \sim 625 K before exposure to methane and recording of the reported Cu Auger LMM spectra.

Figure 8. AP-XPS data associated with the Cu $2p_{3/2}$ region of several samples: (a) 10: 1 Cu@IrO₂, (b) 25: 1 Cu@IrO₂, (c) Cu NWs, and (d) commercial CuO, respectively. The spectra were collected stepwise at 300 K under UHV (black), and at 300 (red), 350 (blue), 400 (green), 450 (purple), and 500 K (yellow) under 30 mTorr of CH₄. The Cu NWs and the Cu@IrO₂ samples were treated in O₂ at ~ 625 K before exposure to methane and recording of the reported Cu $2p_{3/2}$ spectra.

Figure 9. AP-XPS data associated with the Ir 4f region of: (a) 10: 1 Cu@IrO₂ and (b) bulk IrO₂. The spectra were collected stepwise at 300 K under UHV (black), and at 300 (red), 350 (blue), 400 (green), 450 (purple), and 500 K (yellow) under 30 mTorr of CH₄. The Cu@IrO₂ sample was treated in O₂ at ~ 625 K before exposure to methane and recording of the reported Ir 4f spectra.

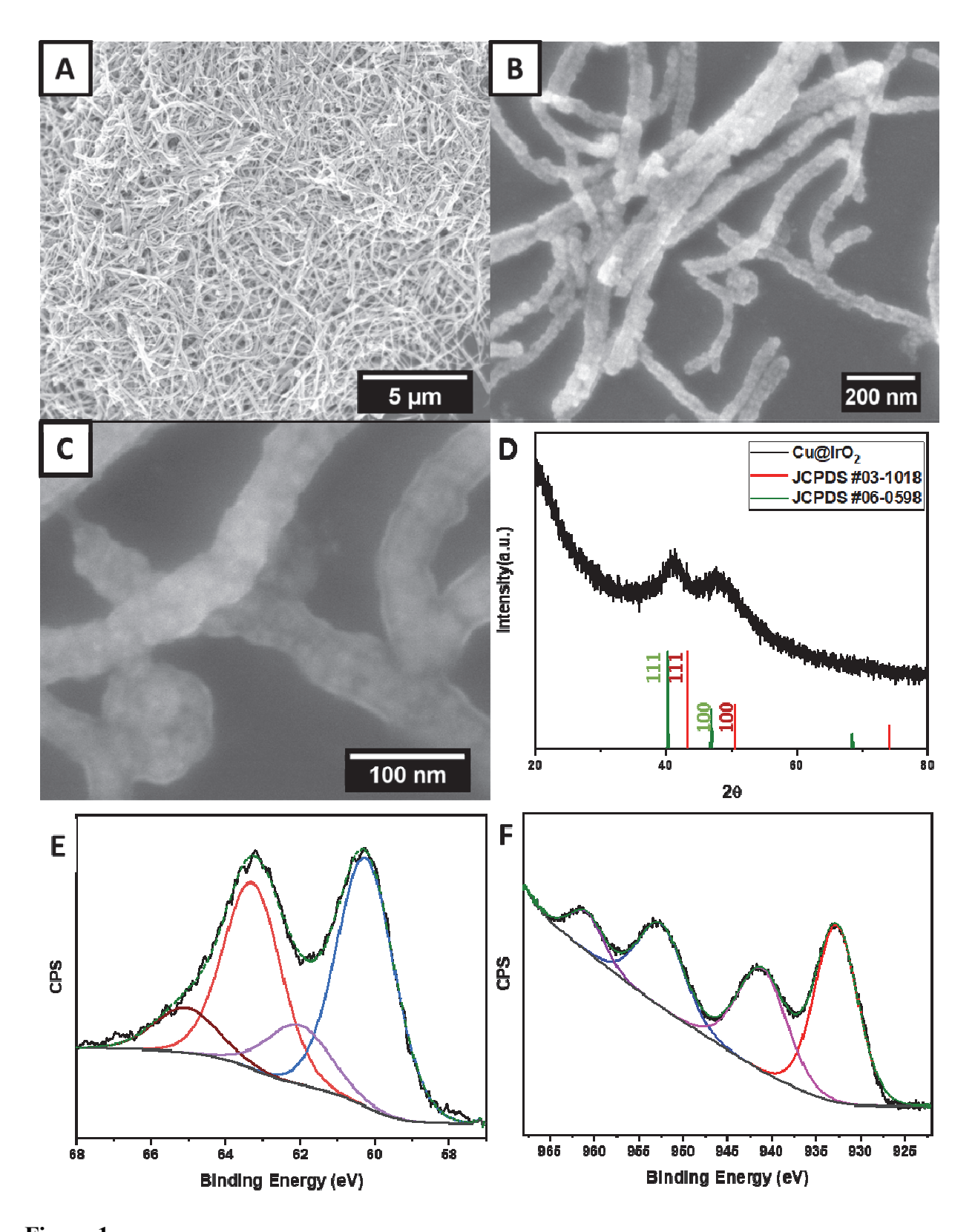


Figure 1.

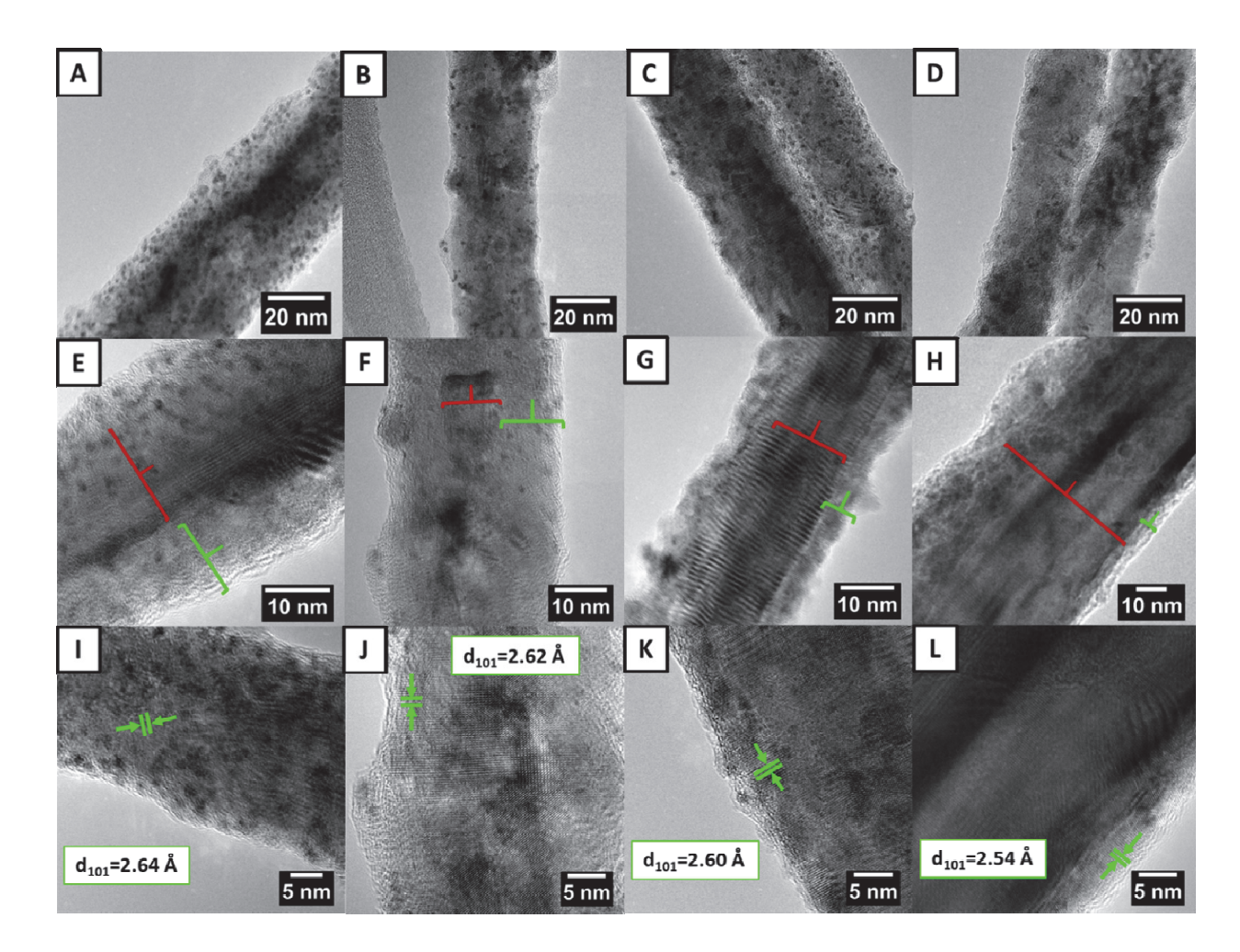


Figure 2. Effect of Varying Cu: Ir Molar Precursor Ratios.

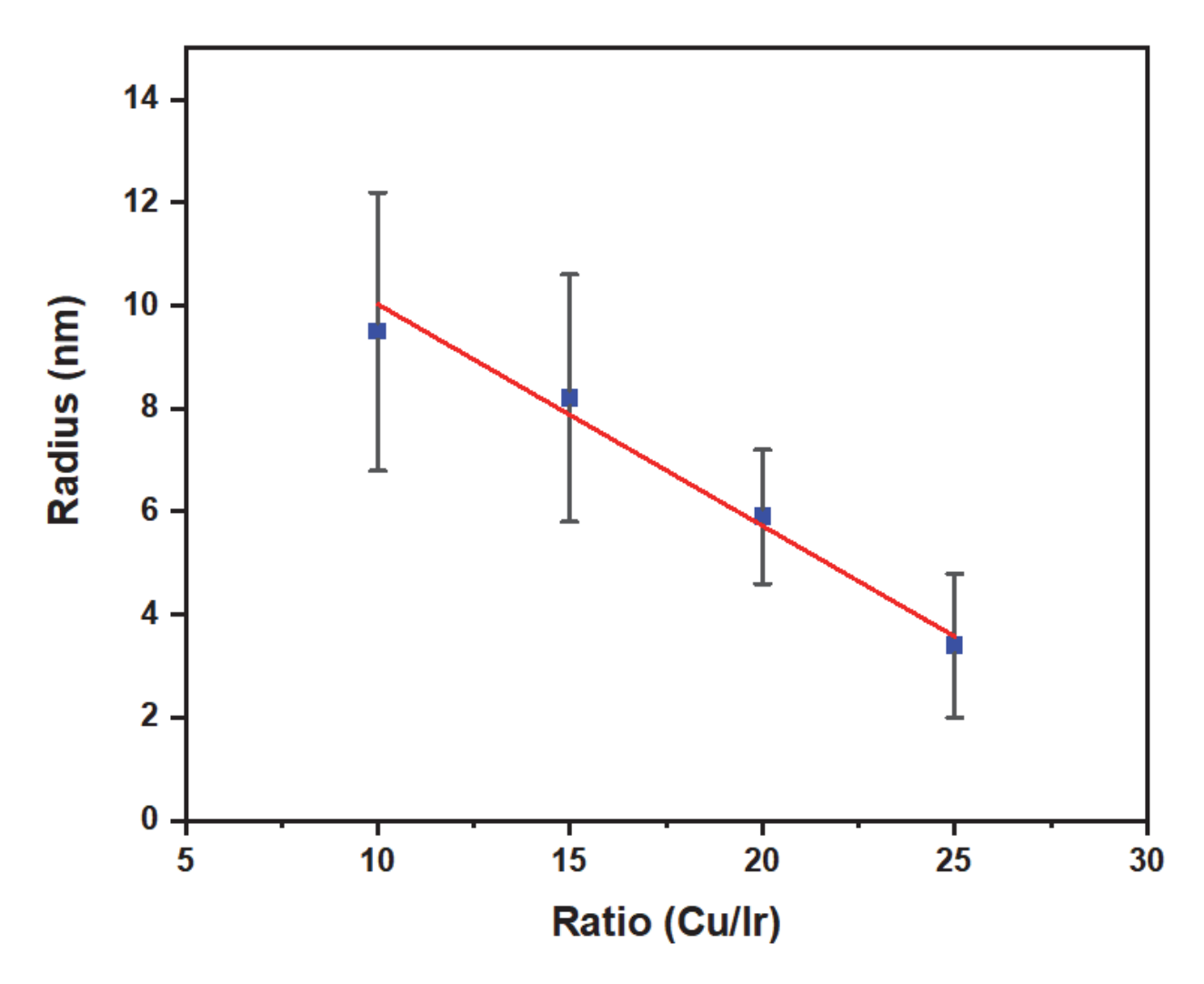


Figure 3.

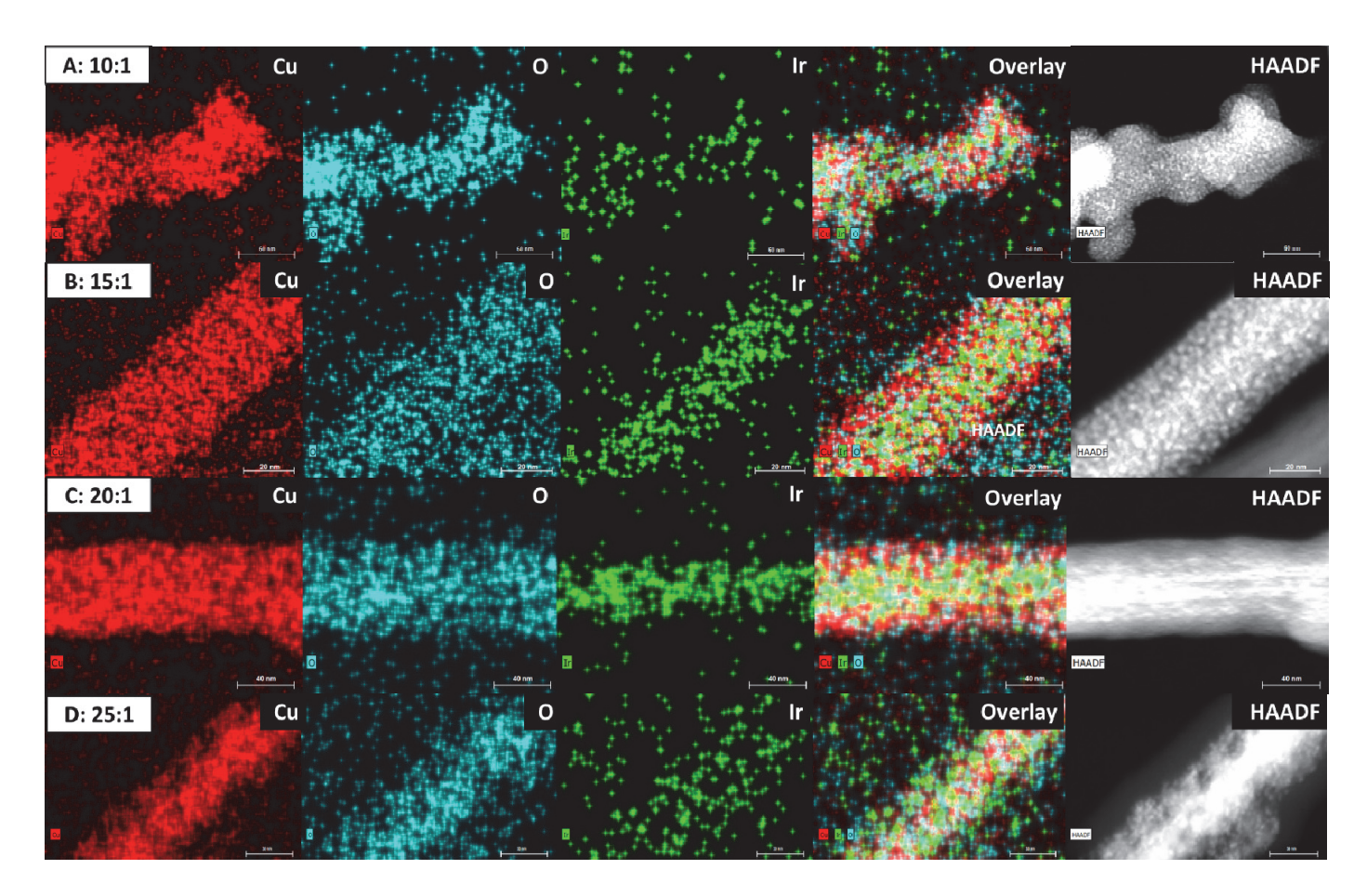


Figure 4.

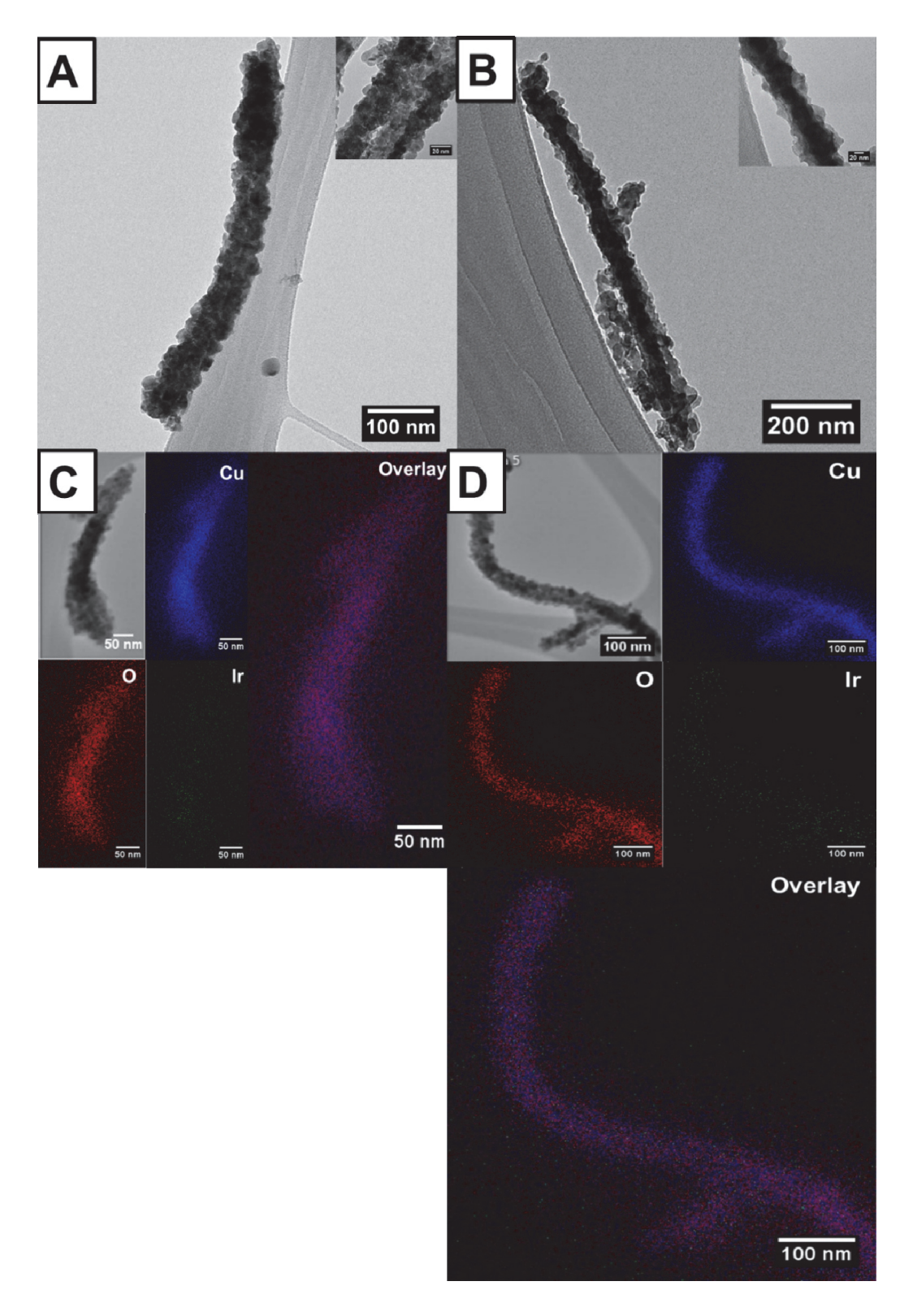


Figure 5. Probing Catalyst Morphology and Composition, (A) Prior to and (B) Subsequent to the Methane Activation Process at 500 K.

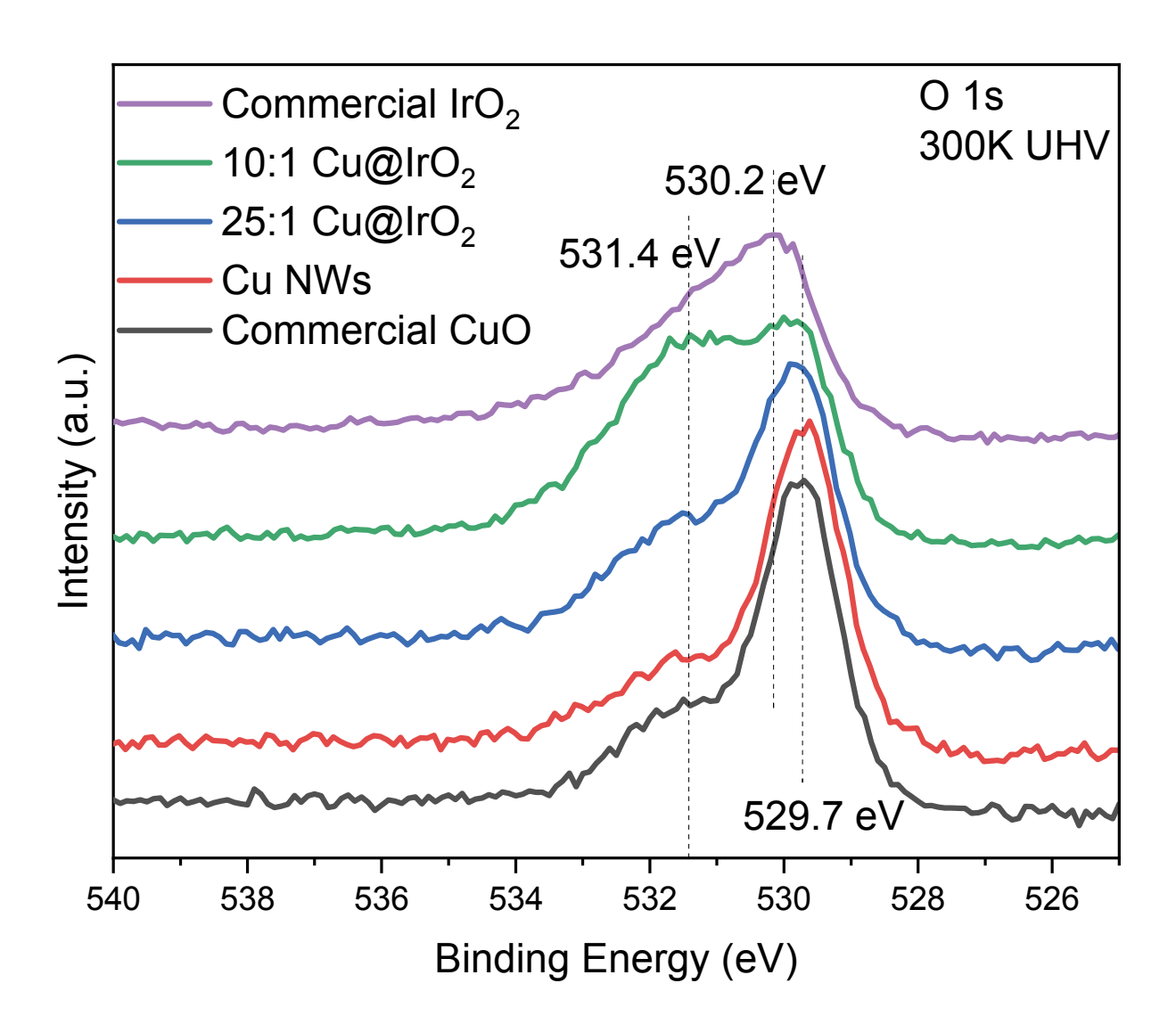


Figure 6.

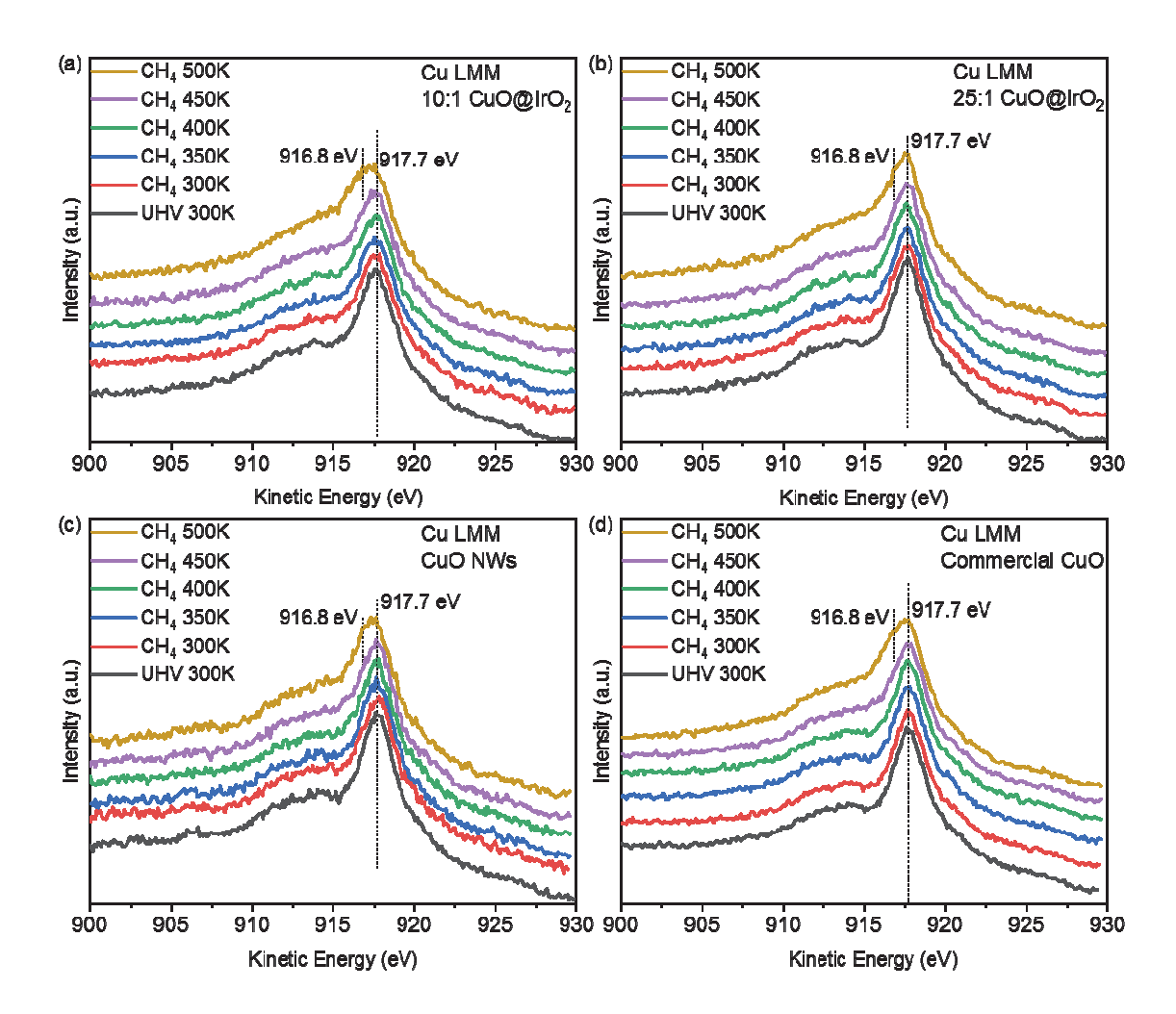


Figure 7.

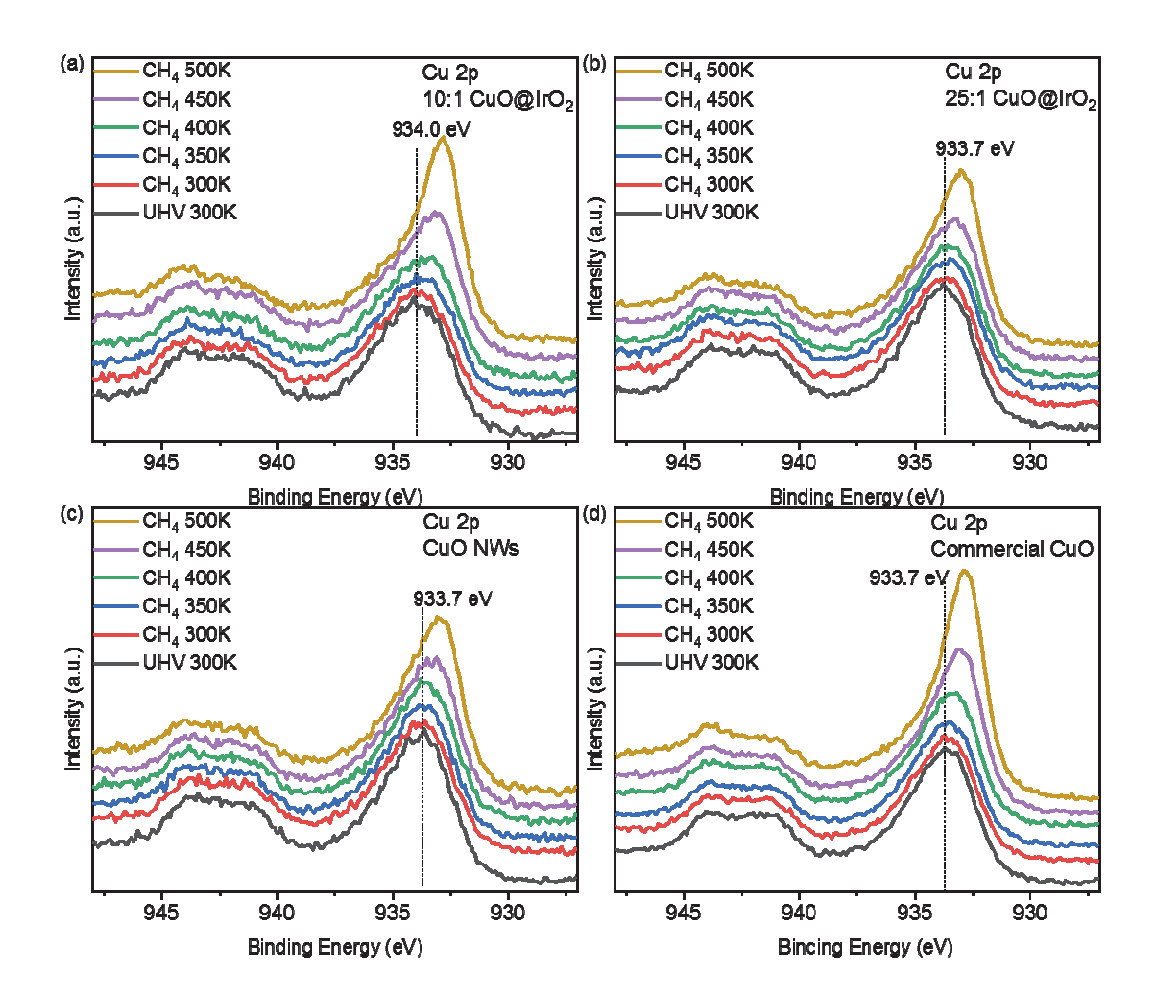


Figure 8.

.

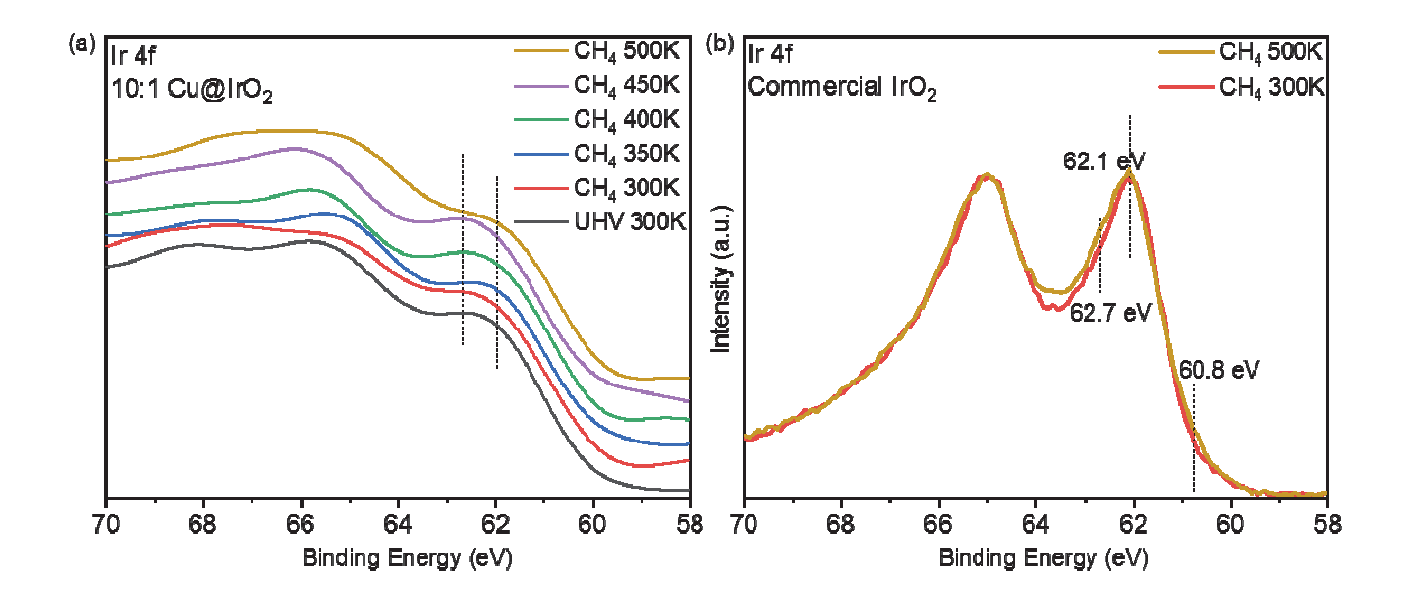
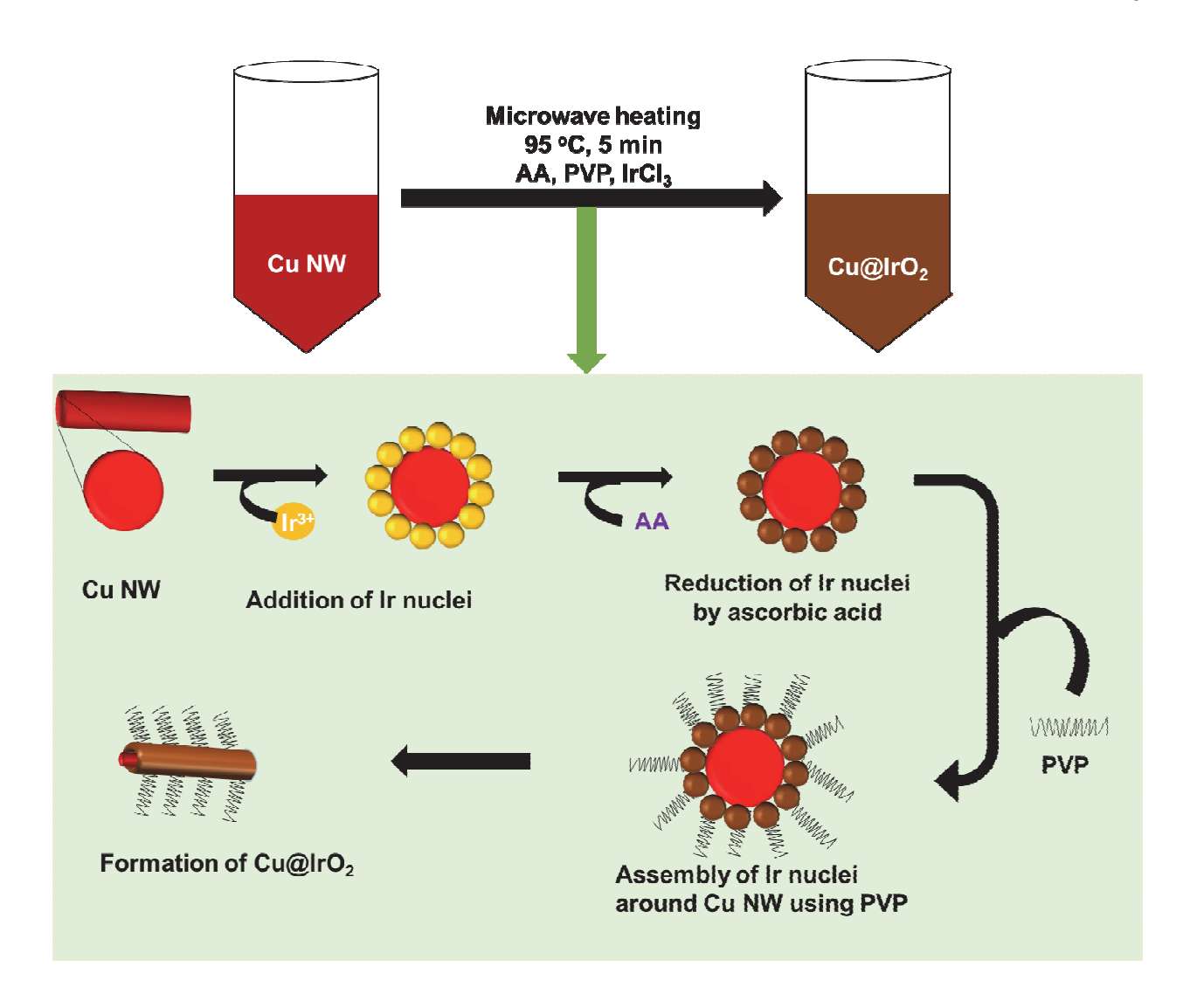


Figure 9.



Scheme 1. Proposed Synthetic Scheme.

Table of Contents Figure

